Pergamon

Geochimica et Cosmochimica Acta, Vol. 65, No. 4, pp. 621–652, 2001

0016-7037/01 $20.00 + .00

PII S0016-7037(00)00521-4

Primary trapped melt inclusions in olivine in the olivine-augite-orthopyroxene ureilite Hughes 009

CYRENA ANNE GOODRICH,[1,*] ANNA MARIA FIORETTI,[2] MARIO TRIBAUDINO,[3] and GIANMARIO MOLIN[4]

[1]Max-Planck-Institut für Chemie, Abteilung Kosmochemie PO 3060, 55020 Mainz, Germany
[2]CNR-Centro Studi Geodinamica Alpina, Corso Garibaldi 37, I-35137 Padova, Italy
[3]Dipartimento di Scienze Mineralogiche e Petrologiche Via Valperga Caluso 35, 10125 Torino, Italy
[4]Dipartimento di Minerologia e Petrologia, Corso Garibaldi 37, I-35137 Padova, Italy

(*Received April* 11, 2000; *accepted in revised form July* 21, 2000)

Abstract—We describe the first known occurrence of primary melt inclusions in a ureilite. The ureilite is Hughes 009, one of a small number of ureilites whose primary mineralogy is olivine-augite-orthopyroxene, rather than olivine-pigeonite. Hughes 009 has a coarse-grained, equilibrated texture typical of ureilites, and homogeneous primary mineral compositions: olivine — *mg* 87.3; augite — *mg* 89.2, Wo 37.0, Al_2O_3 = 1.6 wt.%; orthopyroxene — *mg* 88.3, Wo 4.9. It shows only limited secondary reduction effects and no petrographically recognizable carbon phases, which indicates that its original carbon content was lower than in most ureilites.

The melt inclusions occur in olivine crystals. They are concentrated in the central regions of their hosts, showing elongate (mostly 20–60 μm in maximum dimension), negative olivine crystal shapes and parallel alignment. These and other features indicate that they were trapped during initial growth of their hosts from a liquid, and are likely to be representative samples of that liquid. They consist of glass and single, subhedral crystals of high-Ca pyroxene, with minor Cr-rich spinel and metal-phosphide-sulfide spherules. They are surrounded by halos of olivine with rounded outlines defined by tiny bits of metal and thin arcs of glass. Pyroxenes within each inclusion show zonation patterns indicating that they nucleated at the olivine/liquid interface with compositions close to that of the primary augite, and then grew inward with dramatically increasing Al_2O_3 (to 10.8 wt.%), Wo (to ≈50), TiO_2 and Cr_2O_3 contents. Glasses within each inclusion are relatively homogeneous. Glasses from all inclusions show well-defined trends of CaO, TiO_2, Cr_2O_3, Na_2O and SiO_2 vs. Al_2O_3, (16–23 wt.%) that can be modelled as resulting principally from crystallization of various amounts of the pyroxene. The halos, which represent olivine that grew from the trapped melts, are zoned in Cr and Ca with concentrations decreasing inward, reflecting cocrystallization of pyroxene; they have homogeneous Fe/Mg identical to that of the primary olivine, indicating reequilibration with the host.

We develop a petrologic model for the postentrapment history (crystallization, reaction and reequilibration) of the inclusions, based on which we reconstruct the composition of the primary trapped liquid (PTL). The PTL was saturated only with olivine. This result implies that Hughes 009 is a cumulate (consistent with the high Mn/Mg ratio of its olivine and a low abundance of graphite) and that the composition of the PTL is close to that of its parent magma. The low-pressure equilibrium crystallization sequence predicted by MAGPOX calculations for the PTL (olivine → augite → plagioclase → pigeonite) is not, however, consistent with the primary mineralogy of Hughes 009. If the conditions of these calculations are, indeed, appropriate, then complex processes such as magma mixing must have been involved in the petrogenesis of this ureilite. This conclusion is consistent with other evidence that the olivine-augite-orthopyroxene ureilites record a more complex magmatic evolution than is evident in the olivine-pigeonite ureilites.

TEM investigations of microtextural features in all phases and XRD determination of Fe^{2+}-Mg site distribution in orthopyroxene have elucidated the cooling and shock history of this ureilite. Hughes 009 experienced an extremely high cooling rate (7 ± 5°C/h at the closure T of 630°C) late in its evolution, and two distinguishable shock events—the first at peak pressures of 5 to 10 GPa, resulting in mechanical polysynthetic twinning in augite and orthopyroxene and mild undulatory extinction in olivine; and the second at lower pressures, resulting only in brecciation and redistribution of metal. Its late history is similar to that of most ureilites, and probably reflects impact excavation.

1. INTRODUCTION

A fundamental goal in petrologic studies of igneous rocks is to determine the primary compositions of their parent magmas. This task can be complicated by effects of melt fractionation, crystal accumulation, magma mixing, assimilation, and subsolidus reequilibration. Many of these effects are absent, however, in melt inclusions trapped in early-crystallizing minerals. Melt inclusions that have been shown to be primary (trapped during initial crystal growth) can provide representative samples of the liquids with which their host crystals were in equilibrium (Roedder, 1984; Sobolev, 1996). From studies of such inclusions it is possible to determine the compositions and physical conditions of crystallization (T, p, fO_2) of early melts, and by examining these melts in the context of the host rocks, to gain insight into the course of magmatic evolution. This approach has been successfully applied to a variety of terrestrial volcanic rocks (e.g., Anderson, 1974; Donaldson and Brown, 1977; Price et al., 1986; Roedder, 1976; Rutherford and

*Author to whom correspondence should be addressed (goodrich@mpch-mainz.mpg.de).

Devine, 1988; Sobolev and Danyushevsky, 1994; Sobolev and Shimizu, 1993), to lunar basalts (e.g., Roedder, 1976; Roedder and Weiblen, 1970; 1971; Sobolev et al., 1980), and to cumulate pyroxenite (nakhlite) and dunite (Chassigny) members of the SNC meteorite group (Floran et al., 1978; Harvey and McSween, 1992; Johnson et al., 1991; Treiman, 1993). In this paper, we describe the first known occurrence of primary melt inclusions in a ureilite. These inclusions offer valuable new information about the petrogenesis of a particularly inscrutable group of achondritic meteorites.

Ureilites are coarse-grained ultramafic rocks with equilibrated textures and homogeneous mineral compositions (see reviews by Goodrich, 1992 and Mittlefehldt et al., 1998). The majority (of 95+) are assemblages of olivine and uninverted pigeonite with high (>1200°C) equilibration temperatures. They are depleted in lithophile incompatible elements (relative to chondrites) to a much greater extent than other groups of primitive achondrites such as brachinites, winonaites, or lodranites/acapulcoites, which suggests that they have experienced higher degrees of igneous processing. From a petrologic point of view, they have long been considered to be either cumulates or residues (e.g., Boynton et al., 1976; Berkley et al., 1980; Goodrich and Berkley, 1986; Goodrich et al., 1987). However, they show no correlations between mineral major and minor element compositions (despite comprising a large range in Fe/Mg ratio), such as would be expected in a group of rocks related either by progressive partial melting or by melt fractionation. Likewise, they show no correlation of mineral composition with modal pyroxene/olivine ratio. In addition, they contain little or no interstitial silicate material, and that which does occur may be largely a product of shock-melting and late-stage reduction of the primary olivine and pyroxene, rather than of intercumulus or residual liquids (Mittlefehldt et al., 1998 and references therein).

Moreover, ureilites have a number of properties which are typical of primitive materials and suggest that their parent body has not experienced igneous processing on a sufficiently large scale to annihilate primordial isotopic and chemical heterogeneities. The most striking of these is their oxygen isotopic signature. Unlike other groups of achondrites (even very primitive groups such as brachinites), which show mass-dependent (slope $\approx$ 1/2) $\delta^{17}O$-$\delta^{18}O$ trends indicative of chemical fractionation processes, ureilites define a mass-independent (slope $\approx$ 1) trend similar to the trends shown by chondrites and primitive components of chondrites (Clayton and Mayeda, 1988; Clayton and Mayeda, 1996). Ureilites also show a correlation between oxygen isotopic composition and Fe/Mg ratio, similar to that shown by the ordinary chondrites. This, combined with their near-constant, chondritic Mn/Mg ratios, provides evidence that the large variation they show in Fe/Mg ratio is a primordial feature, rather than a result of igneous fractionation (Goodrich and Delaney, 2000).

These observations have led to petrogenetic models in which ureilites are considered to have formed by limited melting of an isotopically and compositionally heterogeneous (but generally chondritic) parent body (e.g., Scott et al., 1993; Warren and Kallemeyn, 1992). They are argued to be residues rather than cumulates, because cumulate models would require larger bodies of melt (incompatible with preservation of planet-wide isotopic heterogeneities), and furthermore would require a greater number of complementary rock types to be missing from the meteorite record. Other models attempt to reconcile these considerations with cumulate-like textural features of ureilites by envisioning a paracumulate ("mushy, cumulate-like, partial-melt residue") environment of formation (Warren and Kallemeyn, 1989) or emphasizing the aspect of crystal growth from partial melts (Takeda, 1987; Takeda, 1989).

Nevertheless, some properties of ureilites remain difficult to reconcile with single-stage melting models. The most serious problem is their Ca/Al ratios. Goodrich et al. (1987) showed that, in a cumulate model, the Ca/Al ratios of ureilitic pigeonites require derivation from magmas with superchondritic Ca/Al ratios, and therefore from previously igneously-processed (plagioclase-depleted) material. Goodrich (1999a) showed that this problem is not limited to cumulate models. If olivine-pigeonite ureilites are residues from single-stage (<25–30%) melting of otherwise chondritic material, that material must have had superchondritic (2–3.5 $\times$ CI) Ca/Al ratios. Creation of such material by nebular fractionations appears to be even more improbable than generating it by igneous processes, since Ca/Al ratios are remarkably invariant among both bulk chondrites and their components. It is clear that the nature and degree of igneous processing experienced by ureilites, and therefore the means by which their petrologic characteristics can be reconciled with their oxygen isotopic characteristics, remain poorly understood.

Hope to improve that understanding, however, can be found in the 9 ureilites that show the more complex mineral assemblage olivine-augite-orthopyroxene ($\pm$ pigeonite). Six of these show a coarse-grained poikilitic texture typical of heteradcumulates from terrestrial layered igneous complexes (Jackson, 1961; Wager and Brown, 1967), in which olivine and augite are enclosed by large oikocrysts of low-Ca pyroxene (Berkley et al., 1985; Berkley, 1990; Goodrich, 1986; 1999b; Takeda et al., 1989; Weber and Bischoff, 1998). In at least one of these (LEW 88774) it is clear that this is a mineral-melt reaction texture, because augite grains in the orthopyroxene oikocrysts are optically continuous, showing that they are remnants of formerly single crystals (Goodrich, 1999b). Thus, the olivine-augite-orthopyroxene ureilites contain clear evidence of a large melt component and a more complex magmatic evolution than is evident in the olivine-pigeonite ureilites.

Hughes 009 is a 108g meteorite found on the Nullarbor plain of South Australia in 1991 (Wlotzka, 1994). Oxygen isotopic data confirm its identity as a ureilite (Clayton and Mayeda, 1996). It consists of olivine (Fo 87.3), augite (Wo 37) and orthopyroxene (Wo 5), and is the first ureilite known to contain primary melt inclusions (Goodrich, 1998; Goodrich et al., 1999a; b). The inclusions, which occur in olivine crystals, offer the first direct observational evidence concerning the compositions of melts in equilibrium with primary ureilitic minerals. In this paper we present a comprehensive study of the petrology of both the melt inclusions and the primary silicates in Hughes 009, combined with TEM and X-ray diffraction studies which elucidate its cooling and shock history. Our results allow us to address the petrogenesis of this ureilite, and that in general of the olivine-augite-orthopyroxene ureilites.

2. SAMPLES

A 2.1 g sample of Hughes 009 (a freshly-cut slice ≈ 3.4 cm × 4 cm × 3.8 mm in dimensions) was obtained from the Natural History Museum of Bern, thanks to Dr. Beda Hoffman. This sample fell into three pieces. During preliminary examination of the largest (1.04 g) of these, which was free from fusion or weathering crust, we observed a crystal that contained a large number of non-opaque inclusions. A polished thin-section prepared from this surface (B-1) revealed the largest of the inclusion-bearing olivine crystals described in this paper. Section B-2, a polished thick (≈200 μm) section mounted with Canadian Balsam, was prepared from the butt of B-1. The same inclusion-bearing olivine crystal as in B-1 is exposed on both the lower and upper surfaces of B-2 (the lower surface was directly adjacent to the surface of B-1; the observations reported here were made on the upper surface). Section B-3, a polished thin section, was prepared from a surface parallel to B-1 and B-2 and separated from B-2 by ≈2 mm. Section B-3 did not contain the inclusion-bearing olivine crystal exposed in B-1 and B-2, but did contain part of a second inclusion-bearing crystal. After electron microprobe analysis, this crystal was chipped off and used for TEM analyses.

The material that was originally located between B-2 and B-3 was crushed and sieved into four size fractions (350–250 μm, 250–125 μm, 126–90 μm and <90 μm). From the 250 to 125 μm fraction, two single crystals of orthopyroxene were selected, based on transparency and optical extinction, for X-ray diffraction and TEM analyses. Several other grains of orthopyroxene and augite were also selected for TEM analysis.

In addition, three polished thin sections of Hughes 009 (4814-1, 4814-2, 4814-3) were kindly provided by Dr. Martin Prinz of the American Museum of Natural History (AMNH). All of the observations reported by Goodrich (1998) were made on section 4814-1.

3. ANALYTICAL TECHNIQUES

3.1. Electron Microprobe Analysis (EMPA)

Compositions of phases in Hughes 009 were determined using the JEOL JXA 8900RL electron microprobe at Johannes Gutenberg Universität in Mainz or (for section B-3 only) the Cameca Camebax electron microprobe in Padova, operating in wavelength dispersive mode. For standard analyses of silicate phases, operating conditions were 15 keV accelerating potential and 10 to 20 nA beam current. Natural and synthetic oxides and silicates were used as standards. Counting times ranged from 10 to 40 s. PAP $\phi-\rho$-z corrections were applied to the analyses.

Additionally, high precision analyses of olivine were obtained for comparison (particularly of Fe/Mn and Mn/Mg ratios) with the data of Goodrich et al. (1987) for other ureilites. Operating conditions were 15 keV accelerating potential and 200 nA beam current. Counting times were 40 to 60 s for Mg and Fe, and 200 s for Mn, Cr and Ca. Standard deviations obtained were: Mg ≈ 0.1%; Fe ≈ 0.5%; Mn ≈ 0.5%; Cr ≈ 0.1%; Ca ≈ 2%. To ensure consistency of the data with those of Goodrich et al. (1987), the most FeO-rich ureilite (ALH 78019) and the most MgO-rich ureilite (ALH 82130) from that study were analyzed at the same time as Hughes 009. Based on the results of these and other recent 200 nA analyses of these two ureilites, a small correction in Fe/Mg and Fe/Mn ratios was applied to the data of Goodrich et al. (1987). Details of the correction will be published elsewhere.

Analyses of glasses in the inclusions in olivine in Hughes 009 consistently produced totals of only ≈96 to 98%. Test analyses conducted using 5 nA beam current, counting times of 10 s, and (for glasses large enough to permit this) a defocussed (≈5 μm diameter) beam, showed that this was not due to alkali loss. To determine whether the low totals were due to other analytical problems, we analyzed a glass standard similar in composition to the glasses in Hughes 009 (ALV-1690-20, kindly provided by Dr. Timothy Grove). Collective results of these analyses showed concentrations of all elements except Al_2O_3 to be within error of published values (Grove et al., 1990). Al_2O_3 values were low by ≈1 to 2% (relative). This small discrepency does not account for the low totals of the Hughes 009 glasses. Additionally, during many of the sessions in which Hughes 009 glasses were analyzed, we obtained totals close to 100% on other unknown glasses. Therefore, we do not believe that the low totals are caused by analytical problems, but rather to the presence of light elements not being analyzed. Analyses by other techniques are planned to resolve this question.

For analyses of metal, phosphide and sulfide, operating conditions were 20 keV accelerating potential and 20 nA beam current. Pure metals, natural sulfides and apatite were used as standards. Counting times ranged from 15 to 60 s. ZAF corrections were applied to the analyses.

3.2. X-Ray Diffraction (XRD) and Transmission Electron Microscopy (TEM)

Opx1 was measured in Torino with a Siemens P4 four circle diffractometer; opx2 was measured in Padova, with a Siemens AEDII diffractometer. In both cases, the collection was done with the θ-2θ scan type technique using graphite monochromatized MoK_α radiation (λ = 0.71073 Å), and the reciprocal lattice was explored up to $\theta \leq 40°$. After the collections, the compositions of the grains were determined from polished sections of the same crystals, using the Cameca Camebax electron microprobe at Padova operating under the conditions described above.

Crystal structure refinements were performed in the space group *Pbca* using the SHELX-97 package (Sheldrick, 1997), starting from the coordinates of the orthopyroxene in Tribaudino et al. (1997) and following the procedures of Pasqual et al. (2000). All Ca and Na retrieved from the analysis was ascribed to the M2 site, while Al^{VI}, Ti and Cr were constrained to occupy the M1 site. Mg, Fe^{2+} and Mn were partitioned between the M2 and M1 sites with the constraints that the total occupancy of each site was equal to 1, that the total of Fe (all present as Fe^{2+}), Mg and Mn was equal to the analytical value, and that Mn partitions in the same way as Fe^{2+}. Atomic scattering curves were taken from the International Tables for X-ray Crystallography (Ibers and Hamilton, 1974). A fully anisotropic refinement was performed using all unique reflections obtained after merging equivalent ones, with a fixed weighting scheme at the end of the refinement cycles. The final agreement factors R_{obs}, calculated on reflections with Fo > 4σ,

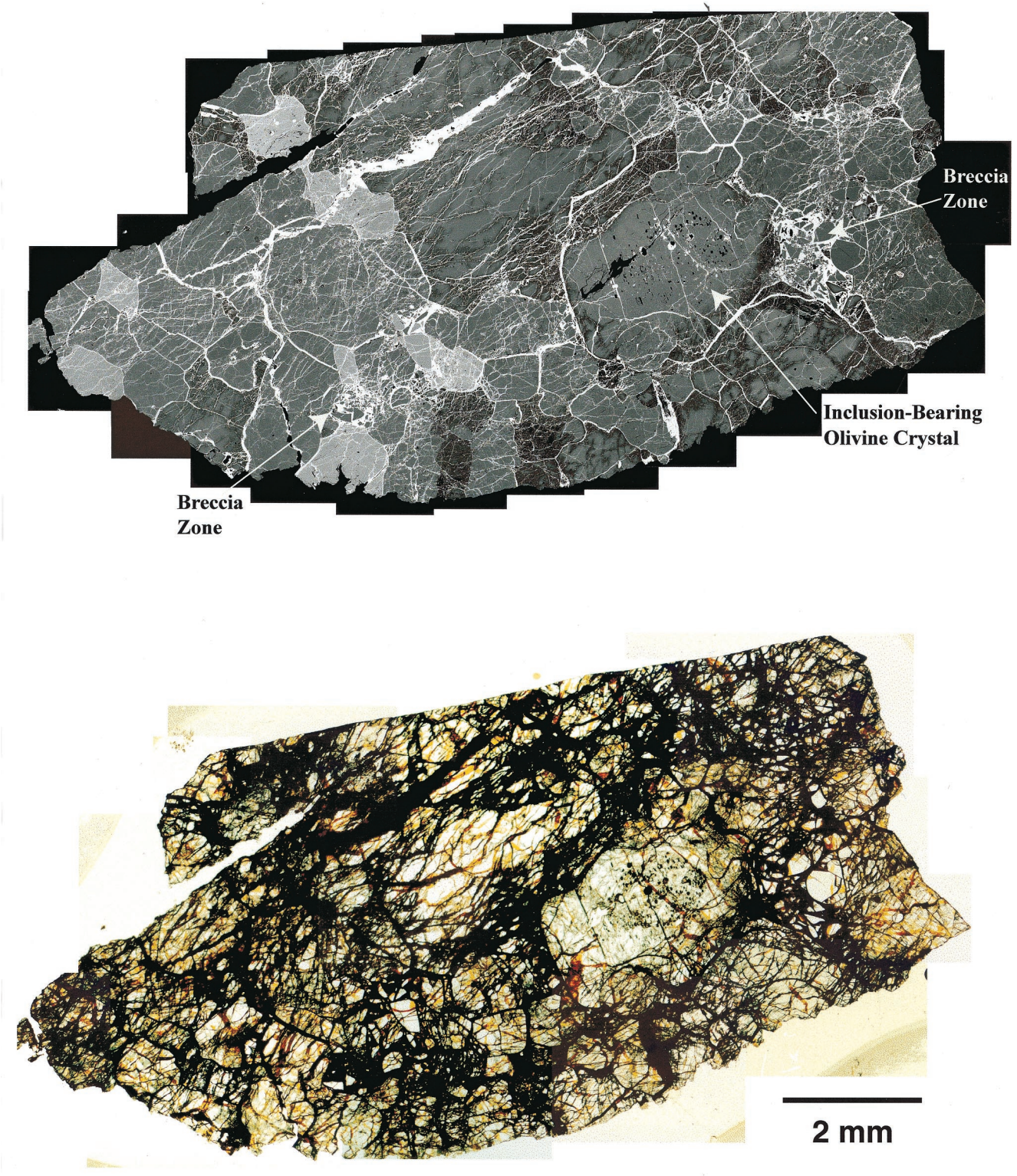

Fig. 1. Thin section B-1 of Hughes 009, shown in collages of back-scattered electron images (top) and plane-polarized transmitted light images (bottom). In the former, light grey grains are augite and uniformly medium grey grains are orthopyroxene. Medium grey grains with darker areas and veins are olivine showing effects of secondary reduction. White (veins, and linings of grain boundaries) = terrestrial iron oxides (presumably replacing metal). Inclusion-bearing olivine crystal (host crystal 1) and areas of severe brecciation are indicated with arrows.

Table 1. Modal abundances of silicates in Hughes 009.

Section	4814-1	4814-2	4814-3	B-2	B-1
Area (mm^2)	75	79	80	78	78
Points	614	6412	5722	4141	7421
Olivine[a]	30	33	36	40	47
Augite[a]	30	11	11	12	7
Orthopyroxene[a]	40	56	53	49	46

[a] Percent.

were 4.2% (opx1) and 2.9% (opx2). The refined occupancies for the two samples fall within error of each other.

Opx1 and a few other orthopyroxene and augite grains, were crushed in an agate mortar and deposited on holey carbon film for TEM analysis. In addition, two samples of the inclusion-bearing crystal removed from section B-3 were ion-thinned and coated with graphite for TEM. Observations were performed with the CM12 electron microscope at Torino, operating at 120 KeV.

4. GENERAL PETROGRAPHY AND MINERAL COMPOSITIONS

4.1. Primary Mineralogy, Textures, and Compositions

Hughes 009 consists of olivine, orthopyroxene (identified both compositionally and structurally), and augite, with minor metal, sulfide, and phosphide. Its primary texture is similar to that of typical ureilites (Goodrich, 1992; Mittlefehldt et al., 1998): silicate grains are subhedral (opx only) to anhedral, with smoothly curving grain boundaries and abundant 120° triple junctions (Fig. 1). Both augite and olivine occur as small, rounded poikilitic inclusions in orthopyroxene. All grain boundaries are lined with Fe-oxides (mostly goethite) assumed to be of terrestrial origin. Metal, intergrowths of metal plus phosphide, and (more commonly) sulfides occur as rare islands in the Fe-oxides, which suggests that they were once a more abundant interstitial component but have been largely destroyed by weathering. No graphite or other carbon-phases, such as commonly occur in the interstitial areas of ureilites, were observed.

Silicate grain sizes, determined from sections 4814-2 and 4814-3, are ≈0.3 to 3.3 mm (avg. of 91 grains = 1.1 mm) for orthopyroxene, ≈0.2 to 1.7 mm (avg. of 32 grains = 0.7 mm) for augite, and ≈0.1 to 2.6 mm (avg. of 35 grains = 0.8 mm) for olivine. These sizes are consistent with those determined for section 4814-1 (Goodrich, 1998). Poikilitic olivine and augite inclusions in orthopyroxene are ≈100 to 200 μm in diameter.

Modal abundances of silicates in section 4814-1 were ≈30% olivine, 30% augite, and 40% orthopyroxene (Goodrich, 1998). Modal abundances determined from four other sections of Hughes 009, by point counting collages of BEIs, are significantly different (Table 1). These four sections contain ≈33 to 47% olivine, 7 to 12% augite, and 46 to 56% orthopyroxene. The only other typical-textured ureilite with an olivine-augite-orthopyroxene mineral assemblage and high abundances of both pyroxenes is FRO 90054/93008 (Baba et al., 1993; Fioretti and Molin, 1996; Tribaudino et al., 1997).

Compositions of the primary silicate minerals in Hughes 009 were determined from sections 4814-1, 4814-3 and B-1 (Tables 2 and 3). Olivine is quite homogeneous, aside from areas which have experienced secondary reduction (see below). The latter were difficult to avoid completely when choosing spots for analysis. Consequently, the average measured *mg* (88.2 ± 1.3 from 112 standard precision analyses; 88.3 ± 0.8 from 54 high-precision analyses) appears to be slightly too high to represent the primary value. For this, we adopt the lowest *mg*

Table 2. Olivine in Hughes 009.

	4814-1 (200 na)[a] (54)	4814-1 (200 na)[a] Most ferroan	4814-1 (81)	B-1 Incl. Xtal[b] (16)	B-1[c] (5)	4814-3 (10)	Grand avg. (112)	Reduction[d] rim (1)
SiO_2	40.32	40.06	40.0	40.0	39.9	40.6	40.1	41.2
	±0.18		*±0.3*	*±0.2*	*±0.1*	*±0.27*	*±0.3*	
Cr_2O_3	0.568	0.565	0.55	0.56	0.57	0.56	0.55	0.52
	±0.013		*±0.03*	*±0.06*	*±0.03*	*±0.03*	*±0.04*	
FeO	11.31	12.29	11.0	12.3	12.2	11.3	11.2	8.4
	±0.74		*±1.2*	*±0.4*	*±0.1*	*±1.1*	*±1.2*	
MgO	47.85	47.33	47.4	46.6	46.7	47.8	47.3	50.3
	±0.60		*±1.0*	*±0.3*	*±0.1*	*±0.8*	*±1.0*	
MnO	0.565	0.562	0.57	0.57	0.57	0.57	0.57	0.55
	±0.010		*±0.02*	*±0.03*	*±0.03*	*±0.03*	*±0.02*	
CaO	0.298	0.302	0.29	0.29	0.31	0.29	0.29	0.27
	±0.006		*±0.01*	*±0.04*	*±0.03*	*±0.03*	*±0.02*	
Total	100.91	101.11	99.8	100.3	100.3	101.1	99.9	101.2
mg	88.3	87.3	88.5	87.1	87.2	88.3	88.2	91.5
	±0.8		*±1.3*	*±0.4*	*±0.8*	*±1.1*	*±1.3*	
Fe/Mg	0.133	0.146	0.130	0.148	0.147	0.133	0.134	0.093
	±0.010		*±0.016*	*±0.005*	*±0.001*	*±0.014*	*±0.016*	
Fe/Mn	19.78	21.59	19.1	21.6	21.2	19.5	19.6	15.1
	±1.48		*±2.1*	*±1.3*	*±1.3*	*±2.1*	*±2.2*	

[a] Columns marked (200 na) are high precision analyses; all others are standard precision (see Analytical Techniques section). Grand avg. is average of only standard precision analyses.
[b] Inclusion-bearing olivine crystal in B-1, exclusive of rims (~25 μm) around inclusions.
[c] Other olivine crystals in B-1.
[d] Most magnesian composition observed in reduction rims.

Table 3. Primary orthopyroxene and augite in Hughes 009.

	Orthopyroxene				Augite			
	4814-1 (90)	B-1 (3)	4814-3 (20)	Grand avg. (113)	4814-1 (65)	B-1 (9)	4814-3 (24)	Grand avg. (98)
SiO_2	55.7 ±*0.3*	55.7 ±*0.2*	56.5 ±*0.2*	55.9 ±*0.4*	53.4 ±*0.2*	53.5 ±*0.4*	54.3 ±*0.2*	53.7 ±*0.5*
TiO_2	0.13 ±*0.02*	0.12 ±*0.02*	0.13 ±*0.02*	0.13 ±*0.02*	0.29 ±*0.06*	0.23 ±*0.03*	0.25 ±*0.03*	0.27 ±*0.05*
Al_2O_3	1.01 ±*0.02*	1.00 ±*0.00*	1.00 ±*0.03*	1.01 ±*0.02*	1.57 ±*0.14*	1.66 ±*0.04*	1.68 ±*0.02*	1.61 ±*0.12*
Cr_2O_3	1.04 ±*0.03*	1.03 ±*0.03*	1.04 ±*0.05*	1.04 ±*0.04*	1.28 ±*0.05*	1.33 ±*0.05*	1.31 ±*0.04*	1.29 ±*0.05*
FeO	7.3 ±*0.1*	7.4 ±*0.1*	7.3 ±*0.2*	7.3 ±*0.2*	4.3 ±*0.2*	4.3 ±*0.1*	4.3 ±*0.1*	4.3 ±*0.2*
MgO	31.0 ±*0.2*	31.1 ±*0.2*	31.5 ±*0.2*	31.1 ±*0.3*	19.6 ±*0.2*	19.8 ±*0.1*	20.1 ±*0.1*	19.7 ±*0.3*
MnO	0.54 ±*0.02*	0.52 ±*0.06*	0.54 ±*0.03*	0.54 ±*0.02*	0.40 ±*0.02*	0.42 ±*0.04*	0.41 ±*0.02*	0.41 ±*0.02*
CaO	2.51 ±*0.03*	2.48 ±*0.04*	2.50 ±*0.06*	2.51 ±*0.03*	18.1 ±*0.3*	17.8 ±*0.2*	18.0 ±*0.2*	18.1 ±*0.3*
K_2O	na	na	na	na	na	bdl	bdl	bdl
Na_2O	na	0.05 ±*0.01*	0.05 ±*0.01*	0.05 ±*0.01*	na	0.27 ±*0.03*	0.27 ±*0.02*	0.27 ±*0.02*
Total	99.2	99.4	100.6	99.6	98.9	99.3	100.6	100.7
mg	88.3 ±*0.2*	88.2 ±*0.2*	88.5 ±*0.3*	88.3 ±*0.2*	89.1 ±*0.4*	89.1 ±*0.2*	89.4 ±*0.3*	89.2 ±*0.4*
Fe/Mg	0.132 ±*0.002*	0.133 ±*0.002*	0.130 ±*0.003*	0.132 ±*0.003*	0.122 ±*0.005*	0.122 ±*0.003*	0.119 ±*0.003*	0.121 ±*0.004*
Wo	4.9 ±*0.1*	4.8 ±*0.1*	4.8 ±*0.1*	4.9 ±*0.1*	37.3 ±*0.7*	36.5 ±*0.3*	36.5 ±*0.33*	37.0 ±*0.7*

ratio determined in the high-precision analyses (*mg* 87.3). CaO and Cr_2O_3 contents of the olivine (0.298 ± 0.006% and 0.568 ± 0.013%, respectively) are high and typical of olivine in ureilites (Goodrich, 1992; Mittlefehldt et al., 1998).

Fe/Mg-Fe/Mn data for the olivine, from the high-precision analyses (Table 2), are plotted in Figure 2, with the trend ($Fe/Mn = 156 * Fe/Mg^{0.94}$) defined by comparable data for (olivine-pigeonite) ureilites (Goodrich et al., 1987) shown for comparison. Overall, the Hughes 009 data show a trend consistent with pure reduction, which reflects the difficulty mentioned above of avoiding reduced areas when choosing spots for analysis. Again, only the most ferroan composition (larger open square) is taken to represent the primary olivine. It is obvious from Figure 2 that this composition is not consistent with the trend shown by olivine-pigeonite ureilites, and has a distinctly higher Mn/Mg ratio. The olivine-augite-orthopyroxene ureilite LEW 88774 (Prinz et al., 1994; Warren and Kallemeyn, 1994; Kallemeyn and Warren, 1994; Goodrich, 1999b) is the only other ureilite known to have a similarly deviant (high Mn/Mg) primary olivine composition (Fig. 2).

As in all ureilites, olivine shows the effects of secondary reduction. These effects are spatially inhomogeneous (Fig. 1): some crystals show reduction only at their outermost edges; others are pervasively reduced along fine, multiply-crosscutting veins (now filled with iron oxide). Compositionally, the extent of reduction is limited to *mg* 91.5, whereas, in most ureilites secondary reduction has produced nearly pure forsterite, independent of primary composition (Goodrich, 1992; Mittlefehldt et al., 1998).

Orthopyroxene and augite (Table 3) are also quite homogeneous: Wo 4.9 ± 0.1, *mg* 88.3 ± 0.2 (113 analyses) and Wo

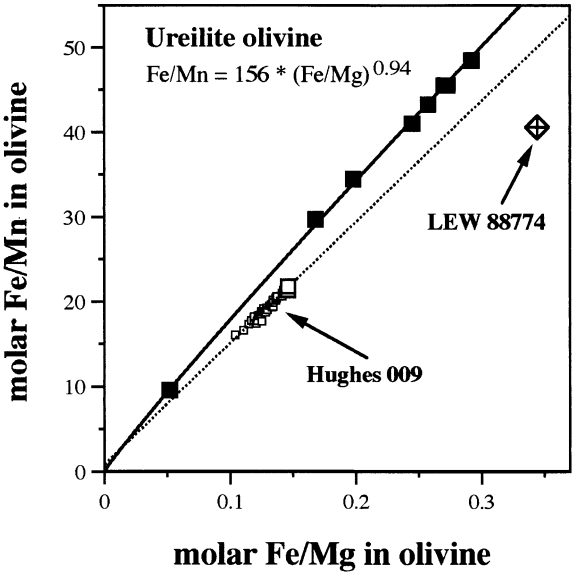

Fig. 2. Plot of molar Fe/Mg ratio vs. Fe/Mn ratio in olivine in ureilites. Filled squares each represent the average composition of primary (unaffected by late reduction) olivine in a single olivine-pigeonite ureilite (both analytical error and internal variation are on the order of the size of the symbols). Data from Goodrich et al., 1987, with slight correction applied based on recent analyses (see Analytical Techniques). Data for Hughes 009 define a trend of pure Fe-loss on this plot (a linear trend passing through the origin), which reflects the effects of secondary reduction. The most FeO-rich composition (open square) is taken to represent the primary olivine composition. Data for olivine in the unusual ureilite LEW 88774 (unpublished data of the first author) shown for comparison.

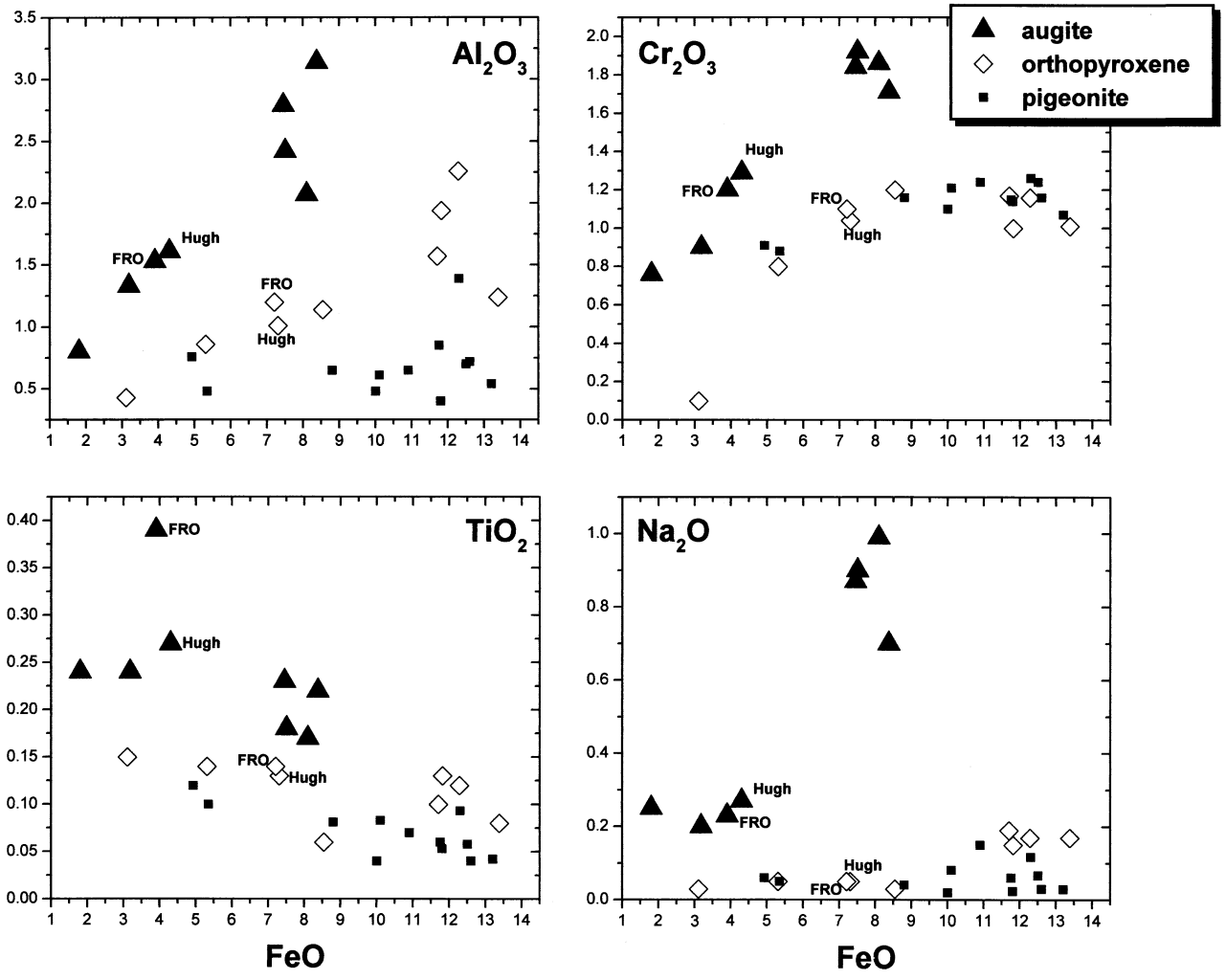

Fig. 3. Minor element contents as a function of FeO content (all wt.%) in ureilitic pyroxenes. Augite and orthopyroxene in Hughes 009 (Hugh) are very similar in composition to those in FRO 90054 (FRO), with the exception of TiO_2 in augite. The set of ureilites containing pigeonite does not overlap at all with those containing augite and orthopyroxene. All those containing augite (8 ureilites) also contain orthopyroxene. There appear to be positive correlations of Al_2O_3 and Cr_2O_3 (and possibly also Na_2O) with FeO content among ureilitic augites, and also of Al_2O_3 with FeO among ureilitic orthopyroxenes. Ureilitic pigeonites show no correlations between minor element contents and FeO. Sources of data: Berkley, 1990; Goodrich et al., 1987; Takeda, 1989; Takeda et al., 1989; Treiman and Berkley, 1994; Weber and Bischoff, 1998; unpublished data of the first author.

37.0 ± 0.7, *mg* 89.2 ± 0.4 (98 analyses), respectively. Their minor element concentrations are shown in Figure 3, with data for augite, orthopyroxene, and pigeonite in other ureilites for comparison. In terms of both major and minor elements, pyroxenes in Hughes 009 are very similar to those in FRO 90054 (Tribaudino et al., 1997), the only exception being TiO_2 in augite, which is significantly lower in Hughes 009. Although pyroxene grains are commonly crosscut by fine (iron oxide-filled) veins like the olivine, they show no reduction along these veins, nor along grain boundaries.

Compositions of the few preserved patches of metal and sulfide that could be analyzed (Table 4) are within the ranges observed for other ureilites (Goodrich, 1992; Mittllefehldt et al., 1998). The metal has very low Cr (0.05%) and relatively low Si (≈0.6%). Sulfide contains ≈4.7% Cr. Phosphide-metal intergrowths are too fine-grained to resolve. Analyses showed

Table 4. Metal and sulfides in Hughes 009.

	Interstitial			Spherules in inclusions		
	(5)	(1)[a]	(1)	(1)	(1)	(1)[b]
Fe	97.2 ± 0.5	81.6	56.3	95.9	61.6	83.4
Ni	1.95 ± 0.07	2.6	0.05	1.61	0.01	1.5
Co	0.20 ± 0.03	0.18	0.08	0.24	0.06	0.17
Cr	0.05 ± 0.01	0.07	4.7	0.03	0.34	0.05
P	0.32 ± 0.03	11.64	bdl	0.14	bdl	8.87
Si	0.58 ± 0.09	0.06	bdl	0.05	0.12	0.05
S	bdl	0.17	36.7	0.02	35.0	0.14
Total	100.3	96.4	97.9	98.0	97.1	94.2

[a] Intergrowth of phosphide and partially oxidized metal.
[b] Intergrowth of phosphide and metal.

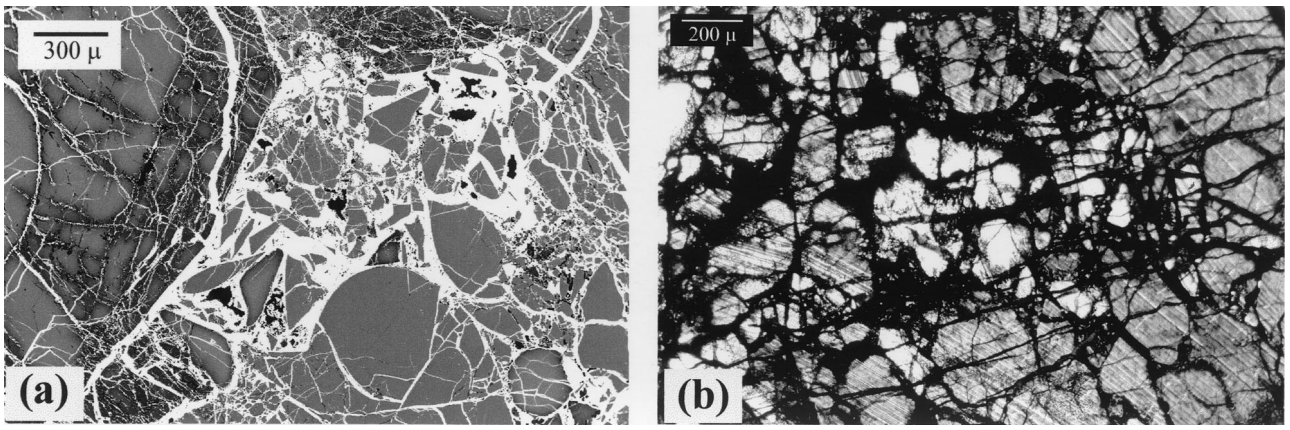

Fig. 4. Brecciated areas in sections B-1 (a) and 4814-3 (b) of Hughes 009. Back-scattered electron image in (a). Plane-polarized transmitted light in (b). Area shown in (a) is indicated in Figure 1. Note that most clasts are highly angular, but a few are well-rounded. Many brecciated olivine grains are completely reduced, others show reduction rims or irregular reduction patterns (a). In (b) an augite grain has been brecciated in situ. Slight displacement of fragments can be seen in offsets of fine twin lamellae.

2.3 to 11.6% P, and suggest that the phosphide is schreibersite (consistent with its optical properties), which has been observed in FRO 90054 and in several other ureilites (Fioretti et al., 1996; Fioretti and Molin, 1998).

4.2. Brecciated Zones and Other Shock Features

The primary texture of Hughes 009 has been disrupted in erratically-located zones in which the silicate grains (particularly olivine) are highly brecciated and the ratio of iron oxide (presumably a replacement of metal) to silicates is much higher than elsewhere (Fig. 4). These zones are broadly vein-like, and in many cases appear to follow primary grain boundaries (Fig. 1). In some places the brecciated grains are small (≈25–50 μm), irregularly-shaped, and densely packed in the iron oxide matrix. In other places there are larger, angular grains that can be reconstructed to form single-crystals with little missing material, or fit back onto grains adjacent to the breccia zone. The fine veins of Fe-oxide (metal) which pervade the rock are more abundant close to the brecciated zones, and appear to emanate from them (Fig. 1). Brecciated olivine grains commonly show secondary reduction (*mg* up to ≈91.5). In the larger grains or clusters this is manifested in a concentric zonation pattern. Smaller grains may be entirely reduced, or show irregular zonation patterns suggesting that they were broken after reduction occurred (Fig. 4a). In other places in the rock, the primary texture is largely preserved, but silicate grains have been brecciated in situ, and now consist of numerous fragments which have little space or Fe-oxide between them

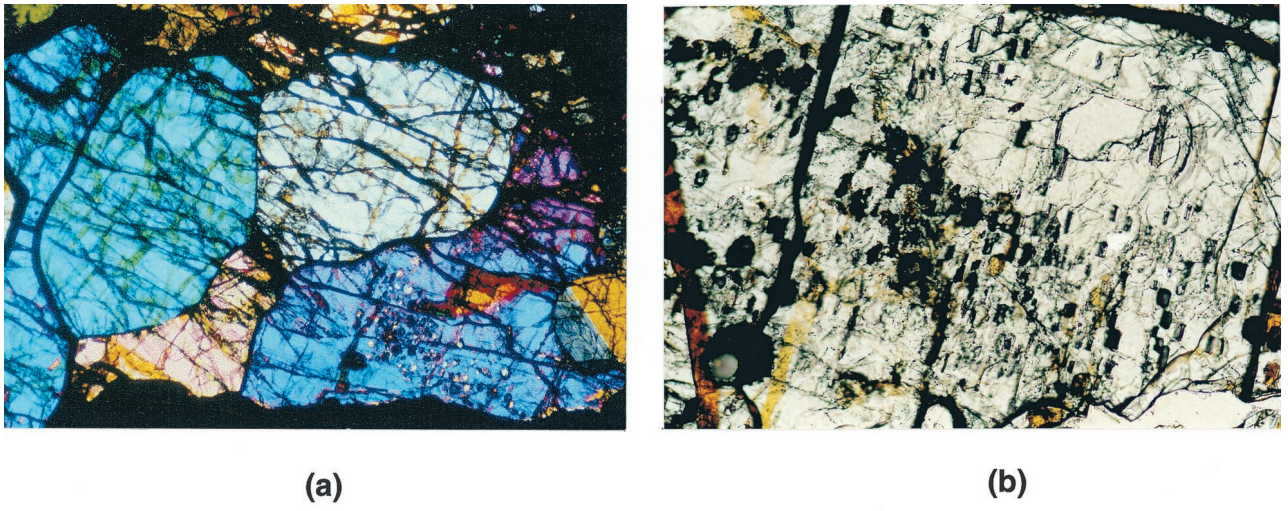

Fig. 5. Transmitted light photomicrographs of inclusion-bearing olivine crystals in Hughes 009. a) Host crystal 3, located on edge of section B-3. Crossed polars. Width of field of view ≈2.3 mm. b) Host crystal 1 in section B-1 (see also Fig. 1). Plane light. Width of field of view = 0.55 mm. Note elongate shapes and parallel alignment of inclusions. Crystals also contain a large number of pits (or pits partially filled with Fe-oxides) that have the same morphologies and alignment and probably represent inclusions that have fallen out or been replaced (dark in these photographs).

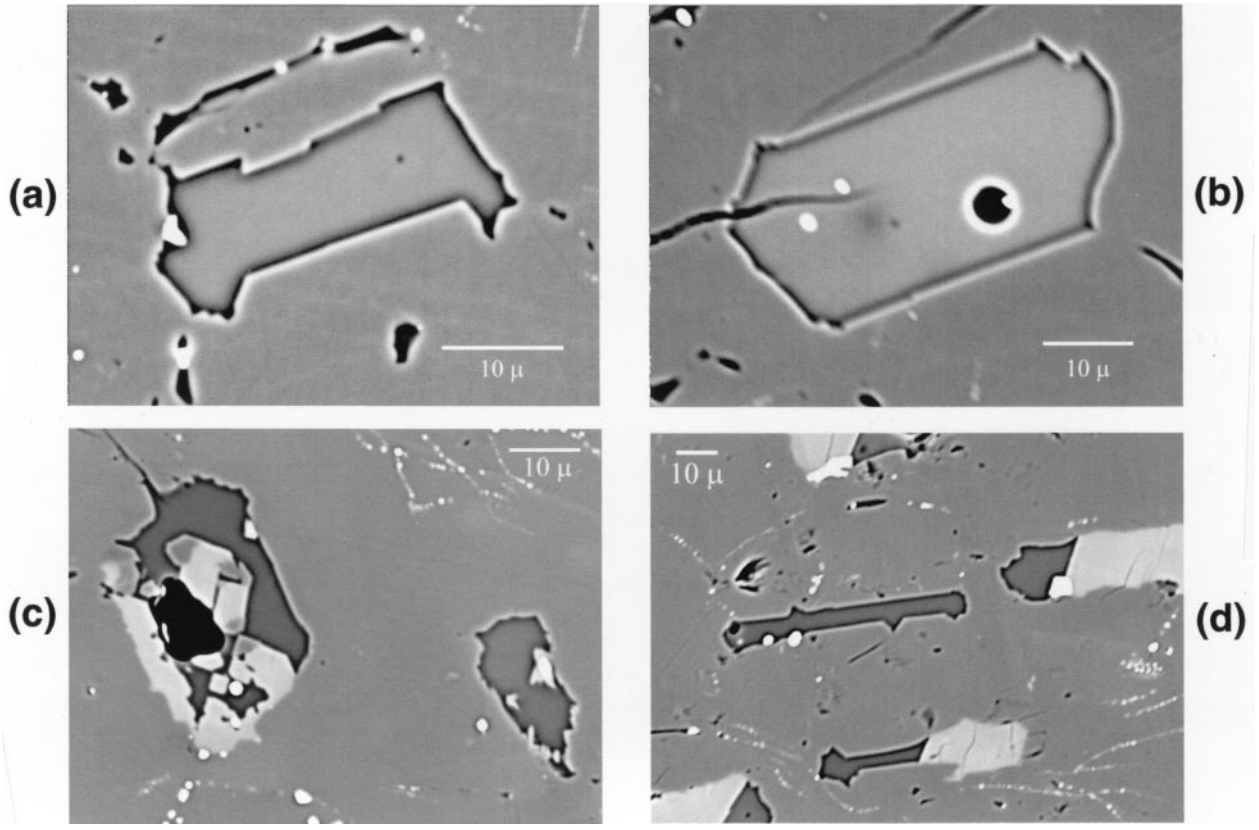

Fig. 6. Inclusions in olivine in Hughes 009 (all host crystal 1 except c), seen in back-scattered electron images. Inclusions in (c,d) contain both high-Ca pyroxene (light grey) and glass (dark grey). Inclusion shown in (c) is one of only two (both in host crystal 2) in which the pyroxene forms rinds and skeletal crystals; darker tips of skeletal crystals are orthopyroxene, observed only in this inclusion. Low-Al_2O_3 glasses (a,b) are lighter than surrounding olivine, while high-Al_2O_3 glasses (c,d) are darker. Small, irregularly-shaped white grains in inclusions (a,c,d) are Cr-rich spinel. Inclusions in (d) are surrounded by olivine halos, defined by tiny grains of metal and thin arcs of glass. Inclusion numbers: (a) 10; (b) 12; (c) 60; (d) 29 (center right), 41 (center left).

but are slightly rotated relative to one another (Fig. 4b). All silicate grains in the brecciated zones are notably free of strain. Olivine fragments in particular are extremely clear, and have sharp optical extinction. In non-brecciated areas, olivine crystals show slight undulatory extinction and a few contain deformation lamellae, and some pyroxene grains show fine striations (Fig. 4b), believed to be polysynthetic twinning.

4.3. Weathering

All three of the AMNH sections contain, in a few places along their outer edges, narrow (≈0.25 mm) rinds consisting of angular to subhedral grains of quartz and lesser feldspar, cemented by rusty iron oxides. These are clearly terrestrial sediments that have adhered to the exterior surface of the meteorite, and are typical for meteorites from the Hughes region of the Nullarbor Plain (Treiman, 1992). None of the sections made from the Bern specimen contain such rinds.

5. MELT INCLUSIONS: PETROGRAPHY AND COMPOSITIONS

5.1. Host Olivine Crystals

Four distinct olivine crystals containing melt inclusions were observed. The largest (host crystal 1) is the crystal observed in hand specimen and now exposed in sections B-1 and B-2. This crystal is subhedral (in contrast to most olivines, which are anhedral), though indented in several places by rounded orthopyroxene grains (Fig. 1). In maximum dimension it measures ≈3.0 mm in B-1 and 2.8 mm in B-2. Compared with other olivine grains around it, it is relatively unbrecciated and pervaded by few Fe-oxide veins, with secondary reduction effects limited to its outermost edges (Fig. 1). It shows banded extinction, indicating mild strain. The inclusions are located almost exclusively in a central region (constituting ≈45% by area), which also has a subhedral morphology. They are elongate, and aligned parallel to one another (Fig. 5b), exhibiting crystallographic control by the host olivine crystal. We studied 56 inclusions from this crystal (almost all of those large enough for EMPA). In both sections, the crystal also contains a large number of pits that appear to have been inclusions, because they have the same morphologies and alignment as they do (Fig. 5). Some of these are partially filled with Fe-oxides, and one contains an island of metal similar in composition to that within the interstitial Fe-oxides, which suggests that these inclusions were originally filled with (replaced by?) metal.

Section 4814-3 shows a partial olivine crystal (≈1.2 × 1.2 mm in size and located at the edge of the section) which contains melt inclusions. This crystal (host crystal 2) is also

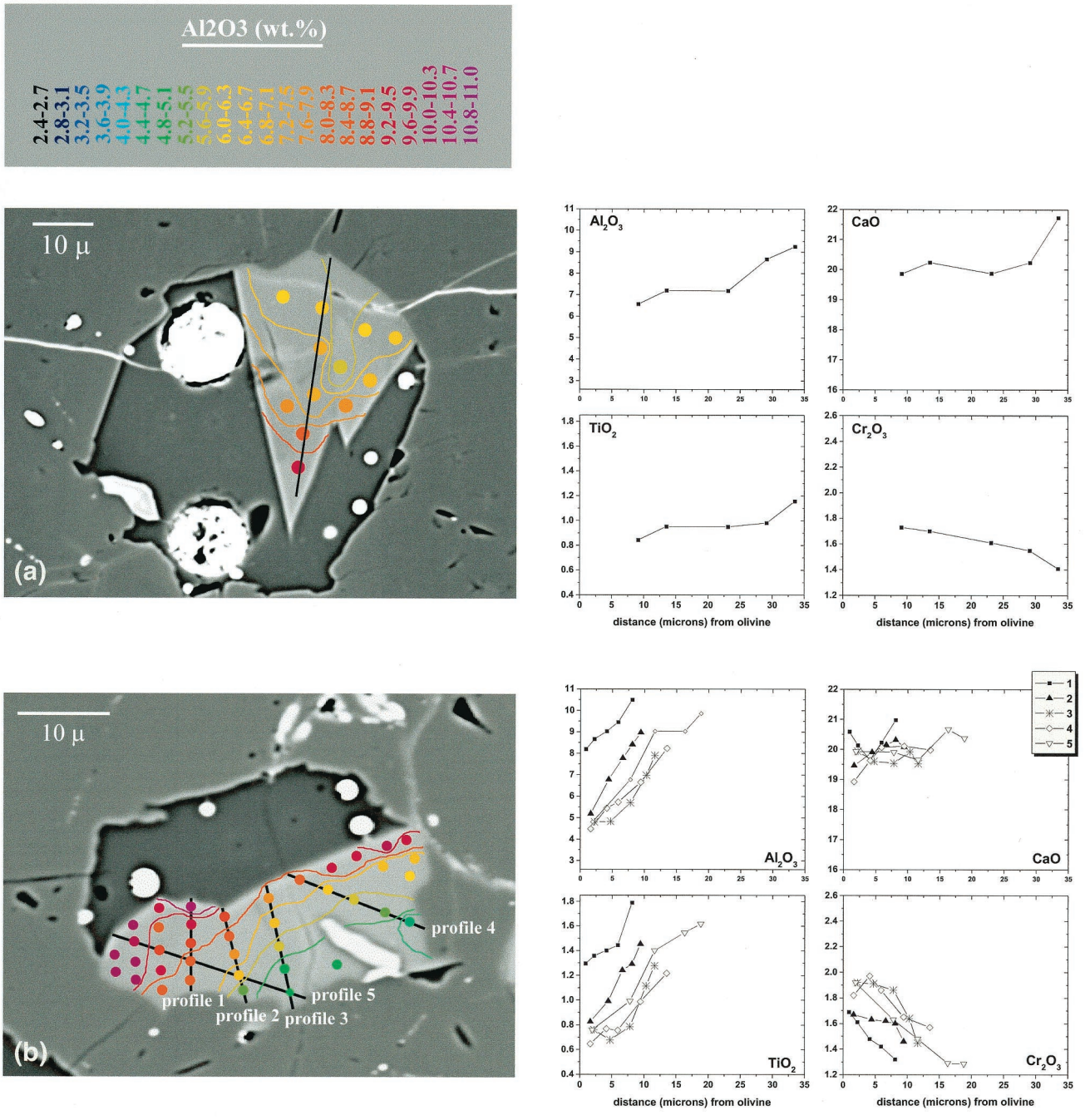

Fig. 7. Compositional zonation of pyroxenes in inclusions. Dots on back-scattered electron images represent analysis points and are color-coded by Al_2O_3 content. Suggested contours of constant Al_2O_3 content have been drawn. Accompanying plots show variation of Al_2O_3, CaO, TiO_2 and Cr_2O_3 content along selected linear traverses (marked on the images). Inclusion numbers: (a) 23; (b) 2; (c) 27; (d) 24.

relatively unbrecciated and free of Fe-oxide veins, with secondary reduction effects limited to its outer edges. The inclusions are elongate and aligned parallel to one another. Only four of them were both sufficiently preserved and sufficiently large for EMPA (roughly three times than many are now partial or complete pits).

Section B-3 also showed a partial olivine crystal (Fig. 5a) containing a few inclusions, located on the edge of the section (host crystal 3). Analyses were obtained from four of these before the crystal was removed for TEM analysis. Two inclusions were found in an anhedral area of olivine adjacent to the main inclusion-bearing crystal in B-2. They are located ≈1 mm from one another, in what is probably a single crystal (host crystal 4) at least 2.75 mm in size.

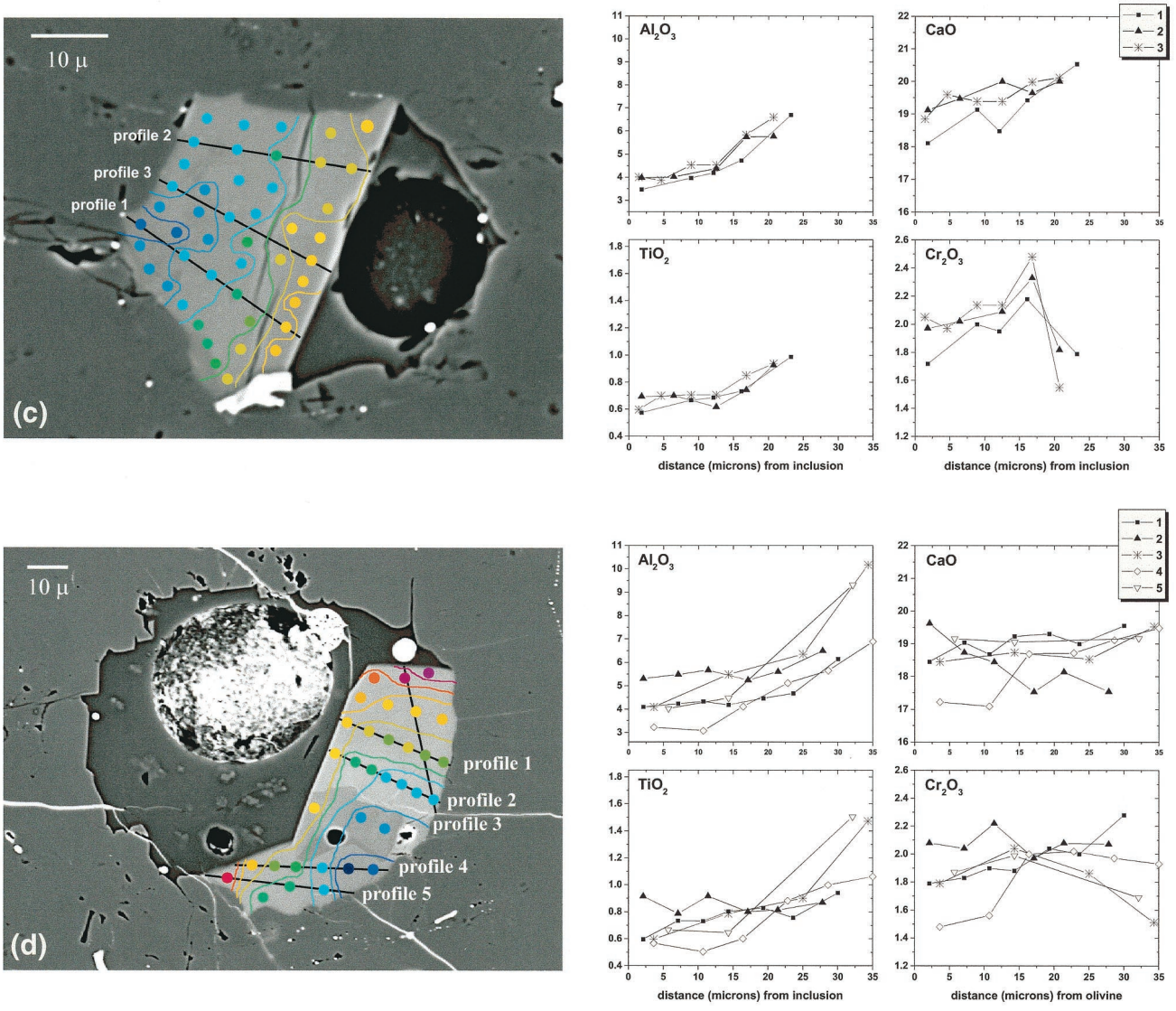

Fig. 7. (Continued)

5.2. Petrography of Inclusions

In thin-section (Fig. 6, 7, 8) the inclusions have maximum dimensions ranging from ≈17 to 97 μm, though most are in the range 20 to 60 μm (mean of 39 inclusions in B-1, B-2, and 4814-3 = 35 μm). Aspect ratios range from ≈1 to 11, but are mostly in the range 1.5 to 3.5 (mean of the same 39 inclusions = 2.1). The inclusions consist predominantly of glass and/or pyroxene. Thirty of the 64 studied showed both pyroxene and glass (though both were not necessarily analyzed because in some cases one, usually the glass, was too small). Thirty-three showed no pyroxene. Only one showed no glass.

In all but two inclusions (both of which are in host crystal 2) the pyroxenes occur as massive single crystals, which are in contact with olivine on two or three sides of the inclusion (Fig. 6d; 7; 8). Where in contact with glass, they exhibit euhedral morphologies. Pyroxene crystals completely surrounded by glass were not observed. In the two exceptional inclusions in host crystal 2, the pyroxene occurs as a rim or partial rim around the glass, and intrudes into it as skeletal crystals (Fig. 6c). Contacts between glass and olivine are sharp (Fig. 6). Along the long dimensions of the inclusions they tend to be straight and/or highly angular. Near the ends or along the short dimensions, the glass commonly appears scalloped, with points projecting into the olivine. In contrast, contacts of pyroxene with olivine are irregular, and more diffuse (Fig. 6c,d; 7; 8).

Cr-rich spinel grains are observed in some inclusions (Fig. 6a,c,d; 7a,b,c; 8a). They are irregular in shape and generally only a few microns in size. In the majority of inclusions, the glass contain spherules, ranging from <1 to 10 μm in diameter, which consist of metal or a metal-phosphide intergrowth, with or without sulfide (e.g., Figure 7a,b,d). It is also common to observe spherical pits (Fig. 7c,d), which may represent metal-sulfide spherules that have been plucked.

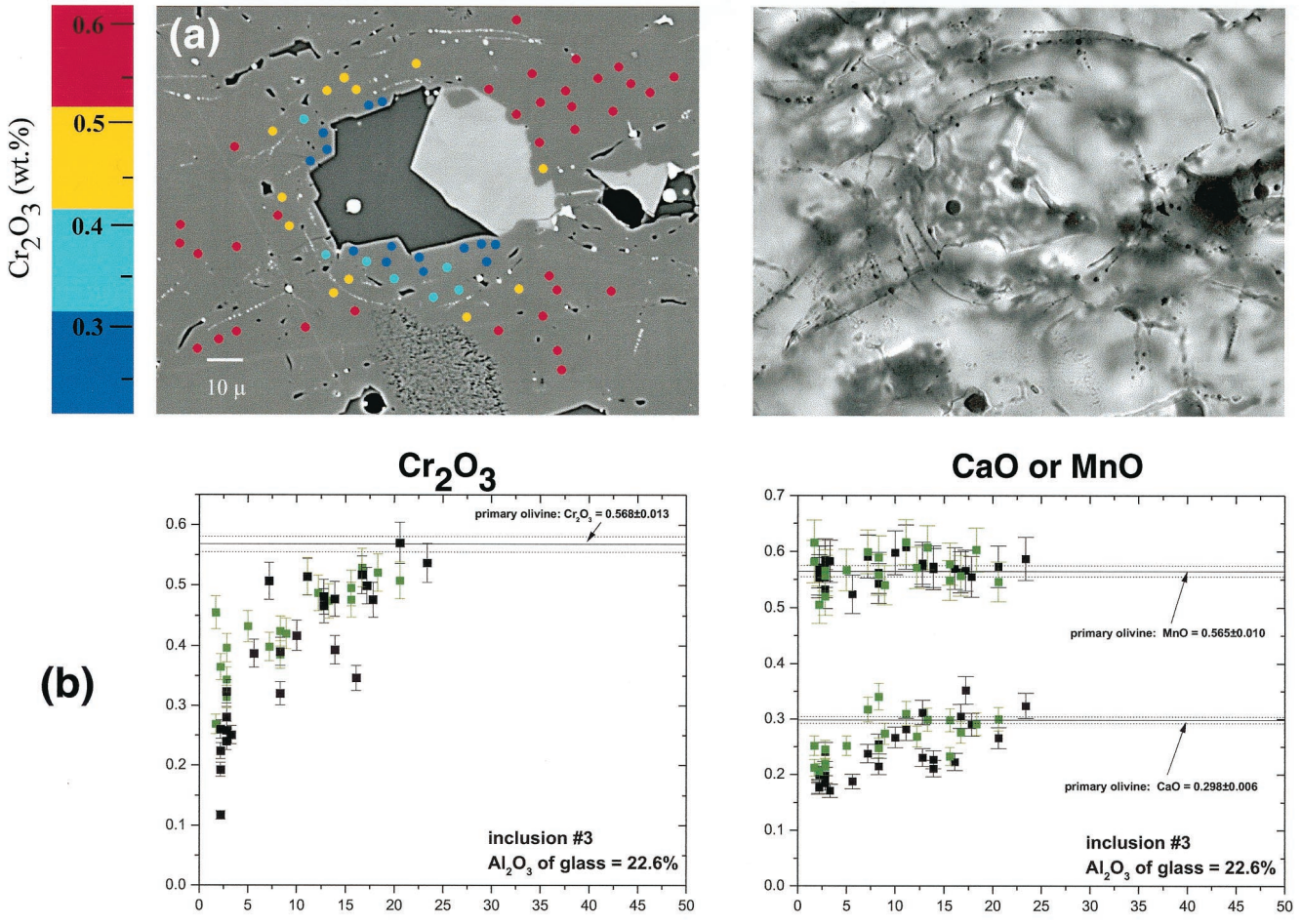

Fig. 8. Zonation of olivine around inclusions. In (a), dots represent analysis points, and are color-coded by Cr_2O_3 content. In back-scattered electron image on left, trace of halo can be seen (tiny metal inclusions forming outline around inclusion). In optical micrograph (plane-polarized transmitted light) on right, halo structure can be seen more fully. Data for this inclusion (#4) are plotted in (c). In (b-d), Cr_2O_3, CaO and MnO contents in olivine are plotted vs. radial distance from inclusion. Black symbols represent points closer to glass than to pyroxene in inclusion; green symbols represent points closer to pyroxene. The four inclusions represented here have glasses with Al_2O_3 contents which cover most of the observed range. Inclusion #5 (d) does not contain pyroxene.

5.3. Compositions of Phases in Inclusions

All data for pyroxene compositions (331 analyses), from 29 crystals (inclusions), are shown in Figure 9. Selected analyses covering the full range of observed compositional variation, are given in Table 5. There was no observed bias in pyroxene composition based on host olivine crystal.

With the exception of one point (the tip of a skeletal crystal in one inclusion in host crystal 2; Fig. 6c) that has the composition of orthopyroxene, the pyroxene is augite. Compared to the primary augite, it has high concentrations of Al_2O_3 (up to 10.8%), CaO (up to 21.9%, Wo ≈50), TiO_2 (up to 1.8%), Cr_2O_3 (up to 2.6%) and Na_2O (up to 0.6%). Overall, the data show well-defined trends of increasing TiO_2, Na_2O and (to a lesser extent) CaO with increasing Al_2O_3, which originate near the primary augite composition (Fig. 9). The variation of Cr_2O_3 with Al_2O_3 is more complex: the data suggest a trend that is first positive and then negative, and show greater scatter than do the other elements. The one orthopyroxene analysis (Wo 3.2) shows extremely high Al_2O_3 (11.4%) compared to the primary orthopyroxene, and also higher TiO_2 (0.65%), but comparable Cr_2O_3 and Na_2O contents (Fig. 9; Table 5). Fe/Mg ratios of the augite (Fig. 9) show little variation: the average value for 330 analyses is 0.136 ± 0.008, slightly higher than that of the primary augite (0.121). The Fe/Mg ratio of the orthopyroxene is similar (0.131), and nearly identical to that of the primary orthopyroxene (0.130). Fe/Mn ratios of the pyroxenes (Fig. 9), scatter slightly around that of the primary augite, and show no correlation with Al_2O_3 content. All pyroxene analyses show good structural formulas (Table 5). Octahedral Al contents are significant, ranging from 0.04 to 0.20 (per 6 oxygen atoms).

For pyroxenes in ten inclusions, more than ten (up to 59) analyses each were obtained. These crystals show large degrees of internal compositional variation, each generally following the overall trends shown by the complete dataset of pyroxenes and, in some cases, covering nearly the full ranges of those

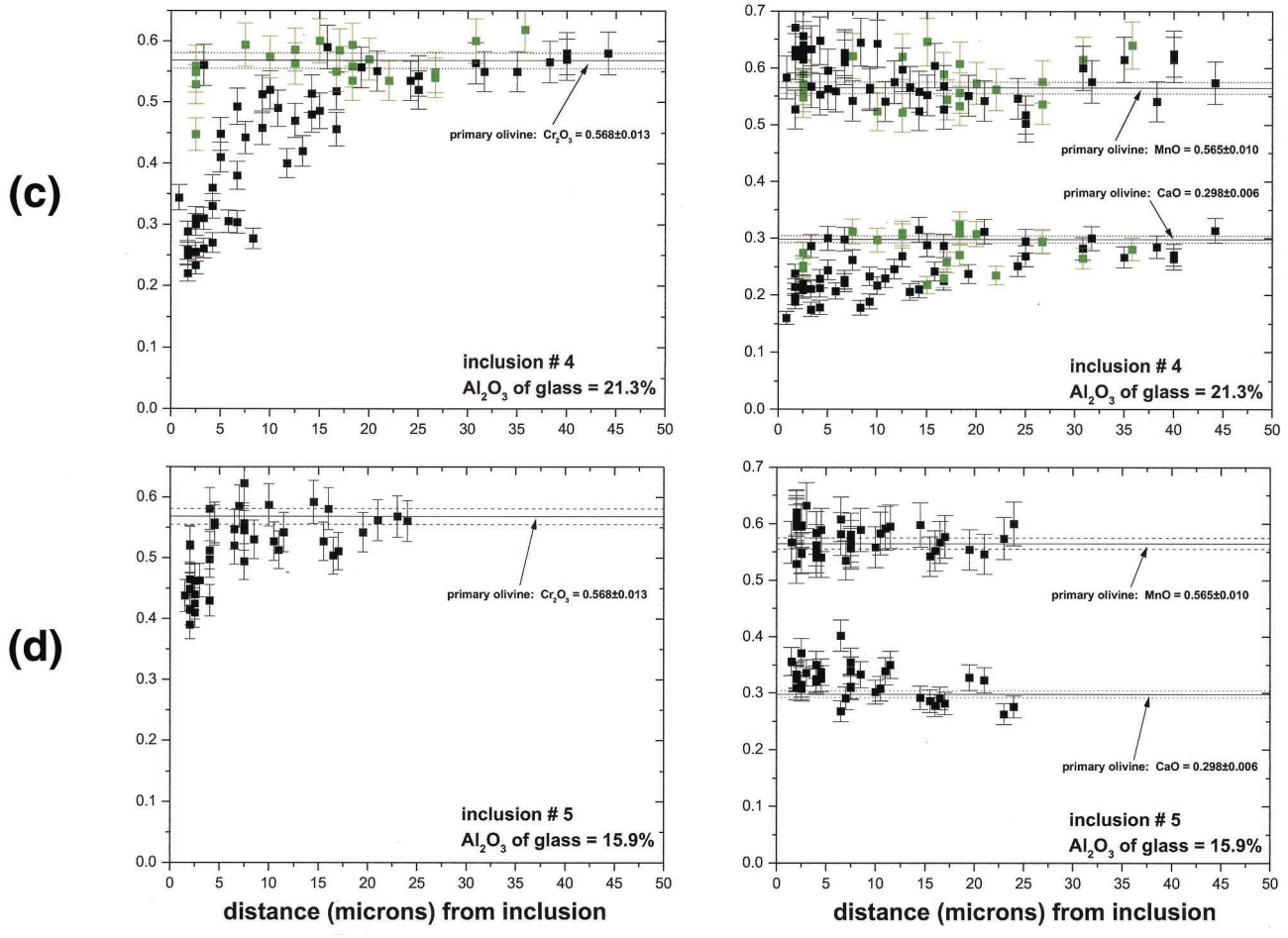

Fig. 8. (Continued)

trends (Table 5). Eight of these pyroxenes were examined for spatial variation in composition. Seven show similar zonation patterns (Fig. 7), in which Al_2O_3 content is lowest (though at various absolute levels in different pyroxenes) at a point along the pyroxene/olivine boundary line which we call the "nucleus." Moving from the nucleus either laterally along the olivine-pyroxene boundary (in either direction), or inward toward the glass, Al_2O_3 content increases. The highest Al_2O_3 concentrations always occur near the pyroxene-glass contact, and often near pyroxene-glass-olivine "triple contacts." In some cases (Fig. 7a,d) the shapes of Al_2O_3 "contour lines" mimic the external morphology of the pyroxene crystal against the glass. Linear traverses were selected for profiling in each crystal, beginning in or near the nucleus and extending toward the glass and/or laterally along the pyroxene-olivine boundary. These profiles (Fig. 7) show that not only Al_2O_3, but also TiO_2 and CaO contents increase in these directions. Cr_2O_3 contents show more complex variation: in some cases (Fig. 7a,b) they decrease continuously along these traverses; in others (Fig. 7c,d) they increase or remain roughly constant and then decrease. The apparent "steepness" of the zonation profiles is variable. The crystal in Figure 7b, for example, shows an increase from ≈4.5 to 10.0% Al_2O_3 over a distance of ≈10 μm, whereas that in Figure 8d remains at ≈4 to 5% Al_2O_3 for a distance of 25 to 30 μm, then increases sharply to >10% in the last ≈5 μm from the glass. The eighth pyroxene that was examined showed little variation in Al_2O_3 content (≈5.0–6.5%), and no regular zonation pattern.

All data for glass compositions (126 analyses), from 55 different inclusions, are shown in Figure 9. Selected compositions (averages for each of 9 inclusions), covering the full range of observed variation, are given in Table 6. Glass within each inclusion is much more homogeneous than the pyroxenes (Table 6) and shows no zonation patterns. Overall, the glasses show a large range of Al_2O_3 content (≈15.3–22.9%), and well-defined trends of decreasing CaO (from ≈15.6–6.2%), TiO_2 (from ≈1.1–0.4%), and Cr_2O_3 (from ≈0.20–0%) and increasing Na_2O (from ≈2.8–4.5%) with increasing Al_2O_3. SiO_2 contents also increase with increasing Al_2O_3 (from ≈55.7–64%). Glasses in host crystals 2, 3 and 4 fall only in the high-Al_2O_3 end of the range shown by glasses in host crystal 1. Fe/Mg ratios of all glasses cluster around an average value of 0.64 ± 0.07, showing a slightly broader distribution than Fe/Mg ratios of the pyroxenes, but no correlation with Al_2O_3 content (Fig. 9). One inclusion in host crystal 2 (one of the two that contains skeletal pyroxene, but not the one that contains orthopyroxene) has glass with exceptionally high Fe/Mg ratio

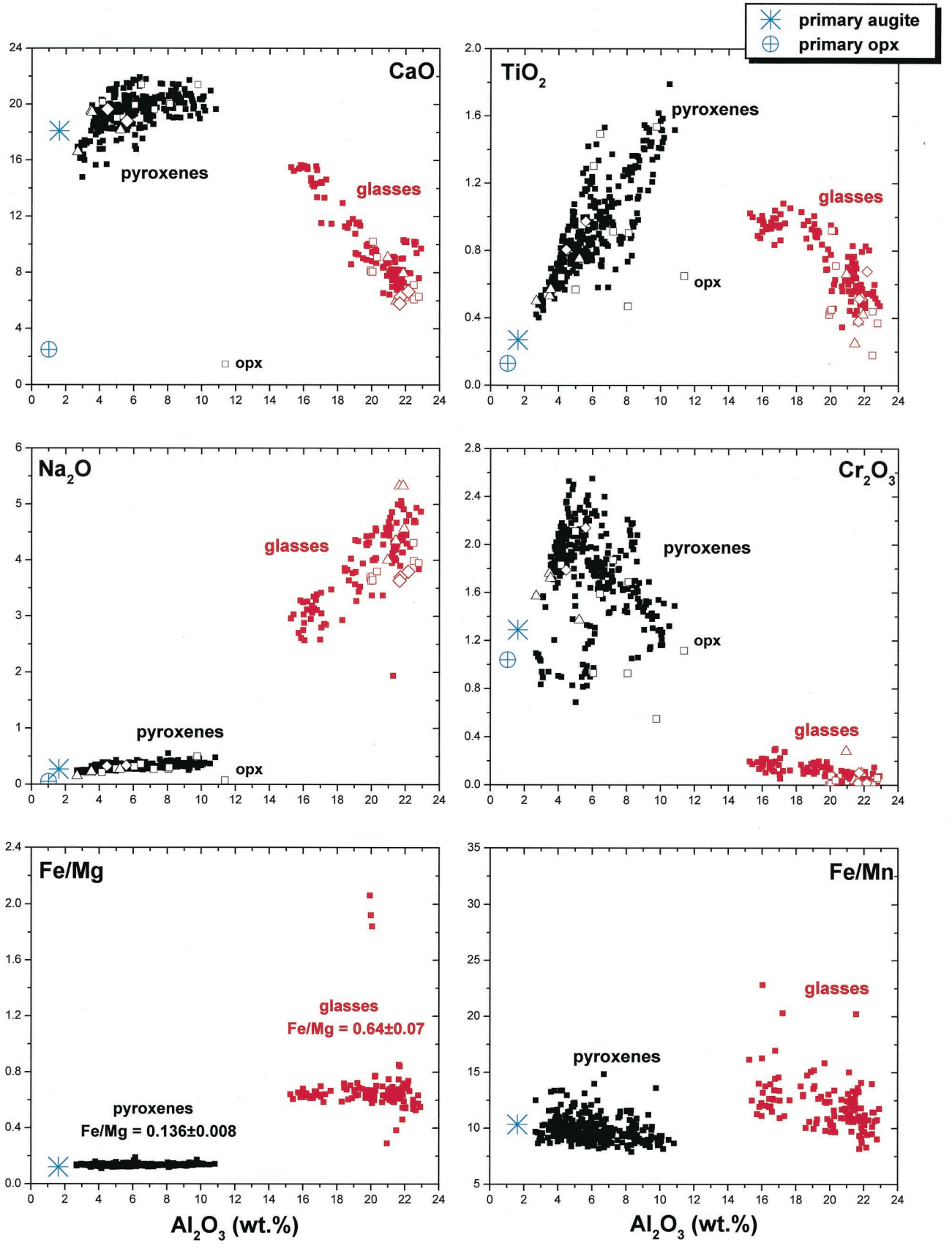
primary augite
primary opx
CaO
pyroxenes
glasses
opx
TiO2
pyroxenes
glasses
opx
Na2O
glasses
pyroxenes
opx
Cr2O3
pyroxenes
opx
glasses
Fe/Mg
glasses
Fe/Mg = 0.64±0.07
pyroxenes
Fe/Mg = 0.136±0.008
Al2O3 (wt.%)
Fe/Mn
glasses
pyroxenes
Al2O3 (wt.%)

Fig. 9. Plots of CaO, TiO_2, Na_2O, Cr_2O_3, Fe/Mg and Fe/Mn as a function of Al_2O_3 for pyroxenes and glasses in inclusions, with primary augite and orthopyroxene shown for reference. Filled squares = host crystal 1; open squares = host crystal 2; open triangles = host crystal 3; open diamonds = host crystal 4. Both pyroxenes and glasses show significant trends for the oxides (wt.%). In contrast, neither show any correlation for Fe/Mg or Fe/Mn (molar) ratio. Pyroxenes have highly equilibrated Fe/Mg, only slightly higher than that of the primary augite (0.121), while glasses show somewhat greater spread. Three glasses with very high Fe/Mg are from one inclusion in host crystal 2. Fe/Mn ratios of pyroxene show a small spread around the value of the primary augite.

(≈1.85–2.0), which is due to exceptionally low MgO contents (Table 6).

No pyroxenes are observed in inclusions whose glasses have Al_2O_3 contents less than ≈19%. Plots of average Al_2O_3 content of glass vs. either average Al_2O_3 or highest Al_2O_3 content in pyroxene (20 inclusions) show positive trends. No attempt was made to look for correlations between apparent pyroxene abundance and either pyroxene or glass composition, because the possibility of unrepresentative sectioning of these inclusions is so high. In addition, no correlation was observed between location in the host and either glass composition or apparent pyroxene abundance.

Only three of the Cr-rich spinel grains observed in the inclusions were large enough for quantitative analysis. Two of these were similar in composition, with *mg* ≈ 70 and molar Cr/(Cr+Al) ratio ≈ 0.33. The other had lower *mg* (≈56) and much higher Cr/(Cr+Al) ratio (≈0.74). Compositions of the metal-sulfide spherules in the inclusions (Table 4) vary. Some spherules consist of sulfide plus low-P (≈0.15%) metal. Others consist of sulfide plus a phosphide-metal intergrowth which was not resolvable. Sulfide in the spherules is distinguished from interstitial sulfides by having lower Cr (≈0.3%).

5.4. Olivine Surrounding the Inclusions

Many of the inclusions are surrounded by round to elliptical halos of olivine, defined by discontinuous trains of tiny metal grains and narrow arcs of glass (at distances of ≈15–30 μm). These features are most prominent optically (Fig. 8a), but can sometimes also be seen in BEIs (Fig. 6d; 8a). In many cases they consist of several concentric outlines or segments of outlines (e.g., Fig. 8a). In places (e.g., Figure 6d), halos associated with adjacent inclusions appear to overlap one another. We believe that these structures represent the original outlines of the trapped melt inclusions, from which olivine grew inward, or growth zones within such olivine. From point-counting of 6 inclusions, using the simplifying assumptions that they are regular elliptical solids, that their olivine shells are uniform in thickness, and that they have been cut along equatorial planes, we calculate the amount of this olivine to range from ≈50 to 95

Table 5. Selected analyses of pyroxenes in inclusions in Hughes 009.

Inclusion[a]	24 (8d)		23 (8a)		27		2 (8b)		3		60 (6c)[b]
SiO_2	52.7	48.4	51.0	48.2	52.3	49.6	49.4	46.4	52.4	49.2	50.2
TiO_2	0.51	1.52	0.79	1.16	0.58	1.10	0.65	1.79	0.42	0.84	0.65
Al_2O_3	3.08	10.82	5.67	9.25	3.47	7.11	4.48	10.50	2.68	6.79	11.4
Cr_2O_3	1.56	1.49	1.33	1.41	1.72	1.69	1.82	1.32	1.09	1.88	1.12
FeO	4.96	3.78	4.30	3.38	4.43	3.56	4.16	3.48	4.84	4.08	6.72
MgO	20.0	14.7	17.5	14.3	18.5	15.5	18.1	14.1	19.7	16.5	28.7
MnO	0.51	0.43	0.48	0.38	0.44	0.35	0.41	0.38	0.49	0.41	0.53
CaO	17.1	19.7	19.2	21.7	18.1	20.4	18.9	21.0	17.0	18.9	1.48
K_2O	bdl	bdl	bdl	bdl	bdl	bdl	bdl	bdl	bdl	bdl	bdl
Na_2O	0.26	0.48	0.29	0.26	0.26	0.37	0.25	0.37	0.25	0.34	0.07
Total	100.7	101.3	100.6	100.0	99.8	99.7	98.2	99.4	98.9	98.9	100.9
mg	87.8	87.4	87.9	88.3	88.2	88.6	88.6	87.9	87.9	87.8	88.4
Wo	35.1	45.7	40.9	49.1	38.3	45.6	40.0	48.4	35.2	42.0	3.2
Structural Formulae (6 oxygens)											
Si	1.90	1.74	1.85	1.76	1.90	1.81	1.84	1.71	1.92	1.81	1.74
Al	0.10	0.26	0.15	0.24	0.10	0.19	0.16	0.29	0.08	0.19	0.26
Sum	*2.00*	*2.00*	*2.00*	*2.00*	*2.00*	*2.00*	*2.00*	*2.00*	*2.00*	*2.00*	*2.00*
Al	0.03	0.20	0.09	0.16	0.05	0.12	0.04	0.17	0.04	0.11	0.20
Ti	0.01	0.04	0.02	0.03	0.02	0.03	0.02	0.05	0.01	0.02	0.02
Cr	0.04	0.04	0.04	0.04	0.05	0.05	0.05	0.04	0.03	0.05	0.03
Fe	0.15	0.11	0.13	0.10	0.13	0.11	0.13	0.11	0.15	0.13	0.19
Mg	1.07	0.79	0.95	0.79	1.00	0.85	1.00	0.77	1.07	0.91	1.49
Mn	0.02	0.01	0.01	0.01	0.01	0.01	0.01	0.01	0.02	0.01	0.02
Ca	0.66	0.77	0.74	0.85	0.71	0.80	0.75	0.83	0.66	0.75	0.05
Na	0.02	0.03	0.02	0.02	0.02	0.03	0.02	0.03	0.02	0.02	0.00
Sum	*2.00*	*1.99*	*2.00*	*2.00*	*1.99*	*2.00*	*2.03*	*2.01*	*2.00*	*2.00*	*2.00*

[a] Inclusion number, with corresponding figure number if available) in parentheses. Most aluminous and least aluminous compositions measured in pyroxene crystal are given for 5 different inclusions.

[b] Orthopyroxene tip on dendritic augite crystal.

Table 6. Selected average compositions of glasses in inclusions in Hughes 009.

Inclusion[a]	6	5	12 (6b)	14	41	1	23	60 (6c)	57
# of points	(2)	(8)	(1)	(4)	(4)	(6)	(3)	(2)	(3)
SiO_2	56.6	56.0	57.1	56.8	59.8	58.7	54.9	61.9	62.7
	±0.2	*±0.2*		*±0.2*	*±0.5*	*±0.6*	*±0.3*	*±0.3*	*±0.1*
TiO_2	0.98	0.95	1.08	0.92	0.56	0.63	0.53	0.41	0.44
	±0.03	*±0.05*		*±0.04*	*±0.07*	*±0.05*	*±0.04*	*±0.05*	*±0.02*
Al_2O_3	15.7	15.9	17.2	19.1	20.2	21.2	21.9	22.6	20.0
	±0.5	*±0.3*		*±0.3*	*±0.1*	*±0.2*	*±0.1*	*±0.2*	*±0.1*
Cr_2O_3	0.17	0.18	0.12	0.16	0.05	0.08	0.05	0.03	0.00
	±0.00	*±0.04*		*±0.03*	*±0.02*	*±0.02*	*±0.03*	*±0.04*	*±0.01*
FeO	2.64	3.06	2.53	2.43	2.11	2.26	2.83	1.58	2.76
	±0.03	*±0.07*		*±0.08*	*±0.07*	*±0.05*	*±0.01*	*±0.01*	*±0.14*
MgO	2.41	2.67	2.42	2.13	1.92	1.98	2.84	1.50	0.80
	±0.01	*±0.07*		*±0.07*	*±0.07*	*±0.09*	*±0.14*	*±0.04*	*±0.02*
MnO	0.20	0.22	0.12	0.19	0.20	0.18	0.27	0.15	0.23
	±0.01	*±0.05*		*±0.03*	*±0.01*	*±0.01*	*±0.01*	*±0.01*	*±0.02*
CaO	15.4	15.5	13.3	11.5	9.5	7.8	10.2	6.2	8.1
	±0.2	*±0.1*		*±0.1*	*±0.1*	*±0.2*	*±0.1*	*±0.1*	*±0.1*
K_2O	0.05	0.04	0.04	0.07	na	0.09	0.04	na	na
	±0.02	*±0.02*		*±0.01*		*±0.02*	*±0.01*		
Na_2O	2.80	2.91	2.86	3.47	4.02	4.17	4.50	3.97	3.68
	±0.33	*±0.22*		*±0.16*	*±0.02*	*±0.19*	*±0.05*	*±0.03*	*±0.04*
Total	97.0	97.5	96.8	96.8	98.4	97.1	98.1	98.3	98.7
Fe/Mg	0.615	0.644	0.586	0.640	0.619	0.639	0.560	0.589	1.94

[a] Inclusion number, with corresponding figure number (if available) in parentheses.

volume percent. None of these assumptions, however, are likely to be strictly true; in particular, the probability that the inclusions are cut along equatorial planes is low, which means that the observed shell/core ratios are unrepresentatively high. We therefore assume that only the lowest of these values (≈50% olivine) could be accurate.

Olivine surrounding (up to ≈45 μm from) twelve inclusions was examined in detail for compositional zonation. Fe/Mg ratios shown by these measurements (401 analyses) are essentially constant (0.146 ± 0.007), and identical to the Fe/Mg ratio of the primary olivine (Table 2). Olivine around one inclusion in section 4814-3 (34 analyses) shows a slightly lower Fe/Mg ratio (0.134 ± 0.003). MnO contents are also essentially constant, and show no significant deviation from that of the primary olivine—0.565 ± 0.010% (Fig. 8).

In contrast, both Cr_2O_3 and CaO show significant zonation, with values decreasing toward the inclusions. In all cases of inclusions that contain both glass and pyroxene, the compositional extent of zonation is greater in olivine surrounding the glass than in olivine surrounding the pyroxene (Fig. 8). In the most extreme cases observed, Cr_2O_3 content decreases from that of the primary olivine (0.568 ± 0.013%) to ≈0.12% close to the glass, and ≈0.27% close to the pyroxene, while CaO content decreases from that of the primary olivine (0.298 ± 0.006%) to ≈0.18% close to the glass and ≈0.21% close to the pyroxene (Fig. 8).

Spatially, the extent of Cr_2O_3 zonation is greater than that of CaO zonation. Cr_2O_3 contents significantly lower than that of the primary value were observed, in the minimum case, up to ≈5 μm from the glass in the inclusion, and, in the maximum case, up to ≈22 μm from the glass in the inclusion. In contrast, CaO contents significantly lower than the primary value were observed, in the maximum case, only up to ≈13 μm from the glass, and, in the minimum case, not at all. In cases of inclusions that have visible halo structures, zonation of Cr_2O_3 and CaO is limited spatially to within the halos and usually does not extend to their outermost zones. In cases where this is not true, there are other inclusions with overlapping halos nearby, making it difficult to decide to which inclusion an olivine analysis should be referenced.

There appears to be a correlation between the degree of zonation around the inclusions and the Al_2O_3 content of their glasses. This is quantified in Figure 10 by plotting the lowest Cr_2O_3 value observed in olivine around an inclusion vs. the average Al_2O_3 content of its glass: the higher the Al_2O_3 content of the glass, the greater the degree of zonation around the inclusion.

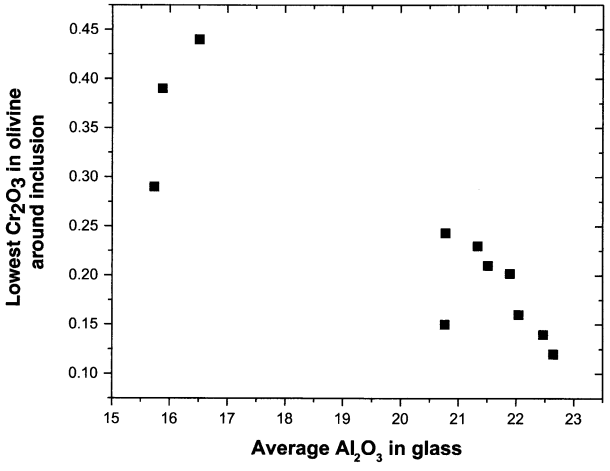

Fig. 10. Plot of the lowest Cr_2O_3 value measured in olivine around an inclusion vs. the average Al_2O_3 content of the glass in that inclusion.

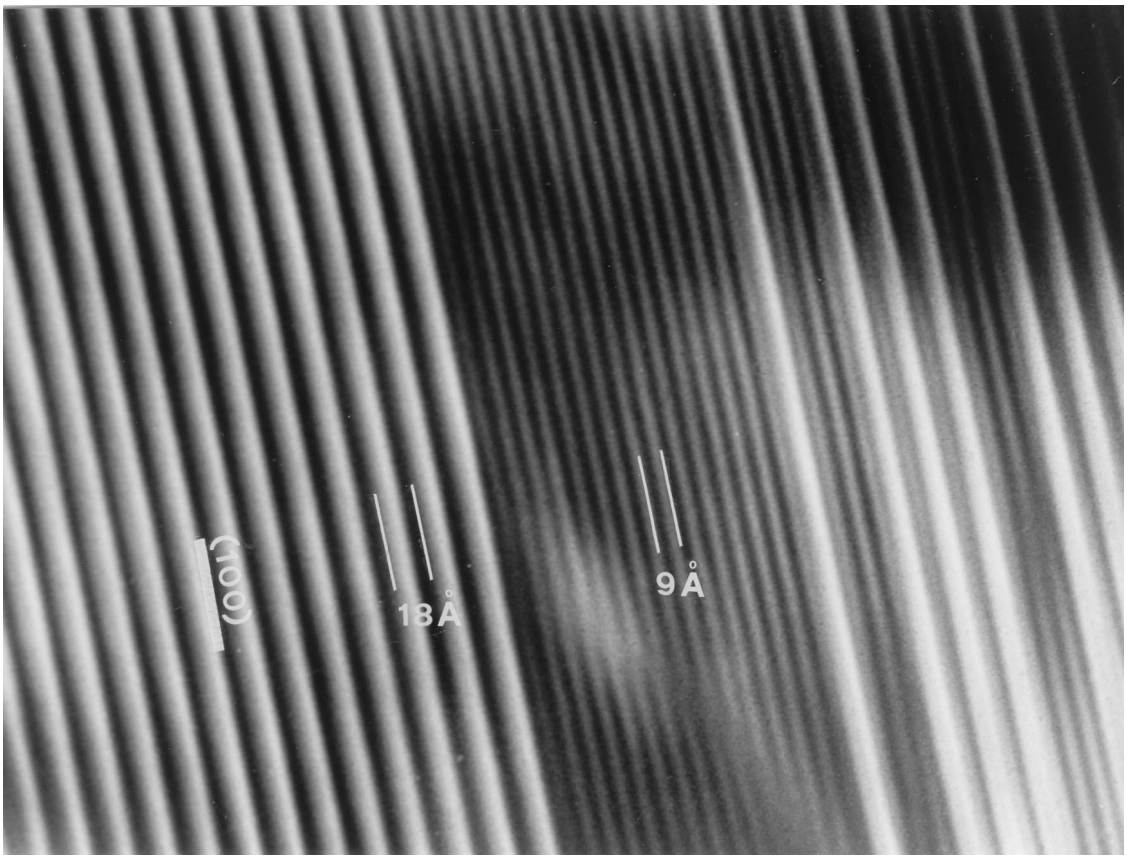

Fig. 11. Lattice image of clinopyroxene lamellae within orthopyroxene matrix. The orthopyroxene 18Å periodicity along a* (best seen at top of photograph) is interrupted by three clinopyroxene lamellae. The lamellae can be recognized by their 9Å periodicity, half that of the orthopyroxene. The thickness of the larger clinopyroxene lamella is 135Å. View along [010].

6. TEM AND XRD OBSERVATIONS

Bright field TEM imaging of the orthopyroxene shows the presence of lamellae, oriented parallel to (100) and 18 −150Å in width. Lattice fringe imaging along a* reveals a lattice periodicity within the lamellae of 9Å (Fig. 11) suggesting that they are clinopyroxene within the orthopyroxene, as previously observed in several ureilites (Takeda et al., 1989; Tribaudino et al., 1997). Their occurence is heterogeneous: some areas of a few μm were found to be free from lamellae, while in other areas the lamellae have average spacings of 200Å or less. TEM-EDS analyses (performed with the minimum spot size of ≈400Å) of areas inside and outside the lamellae showed, within experimental uncertainty, almost a constant composition (*mg* = 88, Wo = 5) consistent with results of EMPA for the orthopyroxene. This, as well as the lack of strain at the interface between clino- and *ortho*- areas, suggests that the lamellae most likely result from partial inversion to clinopyroxene, possibly induced by shock (Takeda, 1989), rather than from exsolution. A similar irregular distribution of shock-induced clinoenstatitic lamellae within orthopyroxene was reported by Brearley and Jones (1998) in shocked chondritic orthopyroxenes. The presence of these lamellae probably explains a slight broadening of the X-ray diffraction peaks observed in the single crystal collection. Slabs with wavy patterns, such as those found by Takeda et al. (1989) in the ureilite Y 74130 and interpreted as related to high shock levels, were not found in Hughes 009.

Results of the single crystal X-ray structural refinement for the orthopyroxene (Table 7) indicate a rather disordered Fe^{2+}-Mg intracrystalline cation distribution, with $k_D(=Fe_{M1}Mg_{M2}/Fe_{M2}Mg_{M1}) = 0.077(\pm 7)$; this value falls within the range of terrestrial volcanic rocks (Fig. 12), and corresponds to a closure T of 630(±24)°C, according to the calibration of Stimpfl et al. (1999) for orthopyroxenes in the compositional range X_{Fe^*} =

Table 7. Selected structural and refinement data and site partitioning for single orthopyroxene crystal (opx2) in Hughes 009.

a (Å)	18.304 (3)	**M1 site**	
b (Å)	8.854 (2)	Mg	0.942 (2)
c (Å)	5.208 (1)	Fe^{2+}	0.020 (2)
V(Å^3)	844.03	Mn	0.001 (2)
N_{obs}	2632	Al	0.005
R_{all}	5.65	Cr	0.028
wR2(%)	8.28	Ti	0.004
Goof	1.04		
		M2 site	
<M1-O>	2.082	Mg	0.699 (2)
<M2-O>	2.186	Fe^{2+}	0.190 (2)
<TA-O>	1.628	Mn	0.013 (2)
<TB-O>	1.640	Na	0.002
		Ca	0.096
Si site			
Si	1.964	k_D	0.077 (7)
Al	0.036	T_c(°C)	630

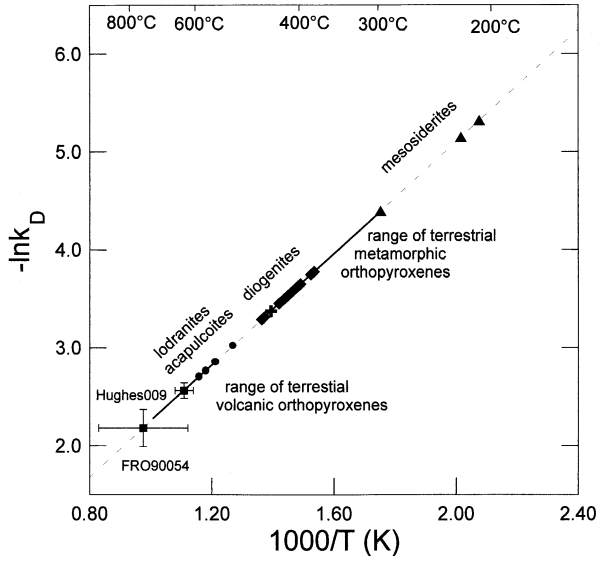

Fig. 12. Plot of $-\ln k_D$ vs 1/T for orthopyroxenes in achondrites. The two ureilites Hughes 009 and FRO 90054 (squares) are clearly affected by higher Fe^{2+}-Mg disorder, indicating faster cooling rates. Other symbols: circles—lodranites-acapulcoites; cross - Sierra de Mage' eucrite; diamonds—diogenites; triangles—mesosiderites. The range found in terrestrial volcanic (within lava flows) and metamorphic orthopyroxenes is shown for reference by bold line. Data: for ureilites from this work and Tribaudino et al. (1997); data for other achondrites from the compilation by Zema et al. (1997).

$0.11 - 0.17$ [$X_{Fe^*} = (Fe^{2+} + Mn)/(Fe^{2+} + Mn + Mg)$; here $X_{Fe^*} = 0.12$].

Bright and dark field observations of the augite show no trace of exsolution lamellae or microtwinning parallel to (100), such as found in FRO 90054 (Tribaudino et al., 1997). Twinning on (100) is indeed present in augite, but only at the optical scale and with a lower frequency. Dark field imaging on the stronger reflections shows the presence of a mottled texture (Fig. 13). In general the texture is non-periodic, but in a few grains, possibly with slightly lower Ca content, a periodicity was revealed by the presence of satellites around the main diffraction peaks. These satellites are oriented along a*, indicating that the main modulation is oriented parallel to (100). Satellite splitting is interpreted as due to incipient spinodal decomposition in clinopyroxenes (Nord and McCallister, 1979; Buseck et al., 1980). The periodicity of the modulation, as estimated by peak splitting, was about 130å, consistent with preliminary stages of spinodal decomposition (Grove, 1982). Similar textures have been observed in natural clinopyroxenes (with $Ca + Na \approx 0.8$) only from the most quickly cooled, fine-grained volcanic rocks (Rossi et al., 1987).

Dark field imaging of clinopyroxenes from the inclusions showed a non-periodic modulation similar to that observed in most grains of the primary augite (Fig. 14). The compositions of these pyroxenes (observed by minimum spot size TEM-EDS) were confirmed to be similar to those determined by EMPA. A few dislocations were observed in the pyroxenes and in the adjacent host olivine. Glass from the inclusions was found to be homogeneous and free of included phases.

7. DISCUSSION

7.1. Melt Inclusions—Reconstruction of the Composition of the Primary Trapped Liquid

The inclusions in olivine in Hughes 009 have typical characteristics which indicate that they are primary and therefore provide samples of the melt from which their host olivines were crystallizing (Roedder, 1979; 1984; Sobolev and Kostyuk, 1975; Sobolev and Shimizu, 1993): they are centrally located in their hosts, they have halos of their host mineral, and they have negative crystal shapes indicating inward growth. Furthermore, they are sufficiently large to provide representative samples of this melt (Anderson, 1974). We will assume that a single trapped liquid composition is represented by all inclusions. This is a good first-order assumption because most of the inclusions studied are located in the same olivine crystal and there is no observed correlation between location in the crystal and glass or pyroxene compositions, so they were probably all trapped at the same stage of melt evolution.

Our principle interest is to determine the composition of this trapped liquid, to gain information about the environment in which the host crystals formed and the petrogenesis of this ureilite. The composition of the primary trapped liquid (PTL) cannot, however, be directly measured, because of the effects of postentrapment crystallization of host and daughter minerals, closed-system reactions, and reequilibration with the host (terrestrial contamination is another possible effect, but we see no evidence for it in the inclusions studied). This is a problem common to most studies of melt inclusions, and various approaches have been taken to solving it. Experimental rehomogenization of the inclusions (e.g., Roedder and Weiblen, 1970; Clocchiatti and Massare, 1985; Sobolev et al., 1980; Sinton et al., 1993; Sobolev and Danushevsky, 1994), combined with suitable corrections for any reequilibration that has occurred with the host (Danyushevsky et al., 2000), can yield both their primary compositions and their entrapment temperatures. Linear regression methods (e.g., Johnson et al., 1991; Harvey and McSween, 1992; Rutherford and Devine, 1988) can be used to mix the enclosed glass and daughter phases computationally with the enclosing host phase, using measured compositions, established mineral/melt partition coefficients, and assumptions about Fe/Mg ratio and saturation state of the primary melt. Alternatively, a two-step approach can be taken, in which the composition of the "visible" part of the inclusion (glass plus daughter minerals) is determined by some method such as point-counting or averaging of rastered- or defocussed-beam EMPA (e.g., Treiman, 1993; Floran et al., 1978; Sobolev et al., 1980). The amount of surrounding host mineral that grew from the trapped melt is then estimated computationally, using constraining assumptions such as the proper Fe/Mg ratio for the primary trapped melt, and/or the requirement that it be multiply saturated with the host mineral and some other phase (e.g., Treiman, 1993; Sobolev and Shimizu, 1993).

Our method for determining the composition of the PTL resembles the latter, but does not rely on integrative methods (point-counting or broad-beam EMPA), which may involve errors resulting from unrepresentative sectioning. Instead, we use the petrographic observations reported above to develop a model for the crystallization, reaction and reequilibration his-

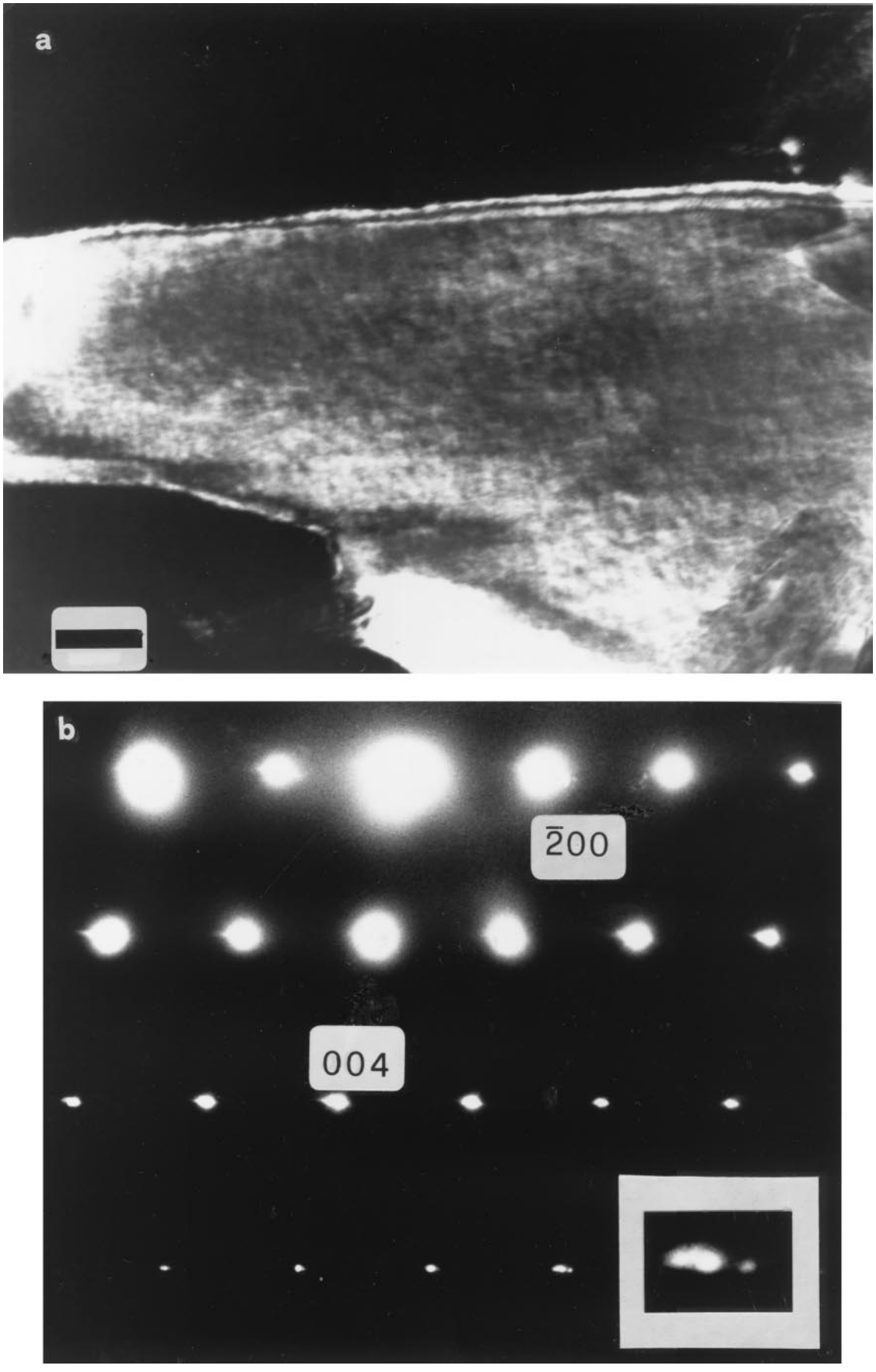

Fig. 13. a) Periodic mottled texture of spinodal decomposition in augite. Dark field, g = [404]. Scale bar: 500Å; b) Selected area diffraction pattern relevant to (a). The enlargement refers to the spot on its left.

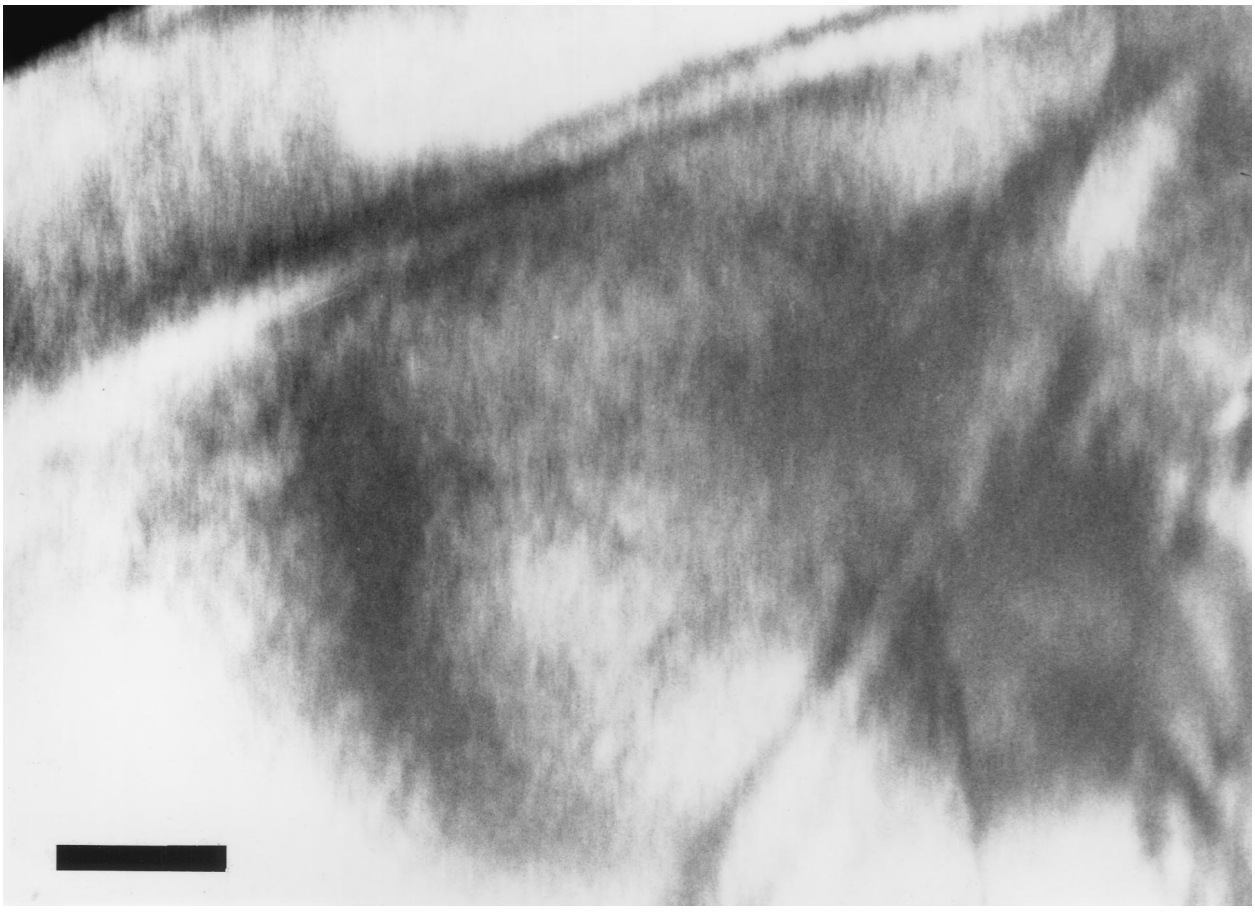

Fig. 14. Mottled texture in a clinopyroxene within glass from an inclusion in olivine. Dark field, g = [131]. Scale bar: 500Å.

tory of the inclusions. We can then reconstruct their original compositions by reversing this history. The key observation which recommends this approach is that the glasses in the inclusions show continuous compositional trends which can be explained principally by crystallization of the observed pyroxenes, so that by extrapolation of these trends we can determine the composition of the trapped liquid before crystallization of any pyroxene. Since pyroxene is the main daughter phase in the inclusions, this accomplishes the largest part of the reconstruction.

Our model for the postentrapment history of the inclusions can be summarized as follows:

$$\begin{aligned}\text{PTL} \rightarrow \text{crystallization of olivine} \rightarrow\rightarrow ? \\ \rightarrow \text{crystallization of pyx} \rightarrow \\ \rightarrow \text{formation of Cr-spinel} \\ \text{and metallic spherules} \rightarrow \text{reequilibration} \rightarrow \text{quenching and} \\ \text{with host} \qquad \text{late reduction.}\end{aligned} \tag{1}$$

In the following sections we discuss the observations that lead to this model, and quantify the reconstruction of the composition of the PTL.

7.1.1. Olivine halos: zonation of Cr and Ca

We believe that the halos of olivine that surround the inclusions grew from the trapped liquids by plating out onto their walls. The tiny grains of glass and metal that define them represent bits of liquid and preexisting metal that were caught at the original olivine-melt interface as olivine began to grow inward. In cases where there are multiple concentric halos, the inner ones reveal growth zones in the inward-growing olivine. The halos, then, provide direct observational evidence, which is not available in most cases of melt inclusions (e.g., Treiman, 1993), as to the amount of host mineral that crystallized from the trapped melts. Furthermore, the zonation of Cr and Ca in olivine within the halos (Fig. 8)

provides information about the crystallization and/or re-equilibration history of the inclusions.

This zonation cannot be due to fractional crystallization of the olivine itself: since Cr and Ca are incompatible in olivine, fractional crystallization would have led to inwardly increasing concentrations of these elements, the opposite of what is observed. Cocrystallization of Cr-spinel might explain the inwardly decreasing Cr contents of the olivine. However, high Cr_2O_3 contents in the pyroxenes suggest that pyroxene crystallization began before Cr-spinel appeared, and since olivine crystallization clearly began before pyroxene crystallization, it seems unlikely that Cr-spinel was cocrystallizing with olivine. Furthermore, cocrystallization of spinel cannot explain the CaO zonation. Secondary diffusion of Cr and Ca into the inclusions (reequilibration) can also be ruled out because this would have led to steeper zonation profiles around the pyroxene than around the glass (since pyx/ol distribution coefficients are higher than liq/ol distribution coefficients for both Cr and Ca), whereas in fact they are steeper around the glass than around the pyroxene (Fig. 8).

The observed zonation patterns can, however, be explained by cocrystallization of the pyroxene in the inclusions. To support this interpretation, we must show that both Cr and Ca behaved compatibly in the pyroxene. For Ca, the smallest distribution coefficient calculated using Ca contents of the pyroxenes relative to those of the glasses is ≈1. The present Cr contents of the glasses are very low, probably due to the late appearance of Cr-spinel. However, if we assume an olivine/liquid distribution coefficient for Cr of ≈0.8 (Schreiber and Haskin, 1976), then from the Cr_2O_3 content of the primary olivine, we calculate that the original Cr_2O_3 content of the liquid was ≈0.7. This leads to minimum D_{Cr} values for the pyroxenes of ≈1.5. Therefore, crystallization of the pyroxene would have led to decreasing Cr and Ca contents in the liquid, and consequently also in co-crystallizing olivine. Furthermore, the higher degree of Cr (compared to Ca) zonation can be explained by the higher D values of Cr.

Cocrystallization of pyroxene can also explain the observation that the zonation profiles around the glass are steeper than those around the pyroxene. It is obvious that when pyroxene nucleated at any point along the olivine-liquid interface olivine must have stopped growing at that point. Therefore, if pyroxene had nucleated at all points of olivine-pyroxene contact simultaneously, all of the olivine surrounding the pyroxene would have formed before any pyroxene crystallized, and would show no zonation. However (as we show in the next section), pyroxene nucleation along the olivine-liquid interface appears to have spread from a point, so some of the olivine around the pyroxene did cocrystallize with pyroxene. The apparently greater degree of zonation around the glass compared to the pyroxene results, therefore, from the fact that a given radial distance from the glass corresponds to a later time (and higher degree of pyroxene crystallization) than the same distance from pyroxene. This explanation for the zonation of the olivine is also consistent with the negative correlation between the Al_2O_3 content of the glasses (which we argue in the next section corresponds to degree of pyroxene evolution) and the degree of zonation around them (Fig. 10).

We can estimate the relative period of olivine-pyroxene cocrystallization by comparing the total widths of the olivine halos with the widths over which zonation occurs. Because of the possibility of unrepresentative sectioning, we assume that the smallest distance over which zonation is observed is the most accurate representation. After correcting for volumetric relationships, this calculation gives the result that only the final ≈5% of the olivine that grew from the trapped melts cocrystallized with pyroxene.

7.1.2. Pyroxene and glass compositional trends

Although the monocrystalline, subhedral habit of the pyroxenes in the inclusions suggests the possibility that they were preexisting primary grains trapped together with melt (e.g., Harvey and McSween, 1992), several observations make it clear that they nucleated within the trapped melts:

1) As shown above, cocrystallization of pyroxene provides the most likely explanation for the Cr and Ca zonation of the halo olivine.
2) Their contacts with the halo olivine are diffuse and irregular, indicating mutual growth.
3) They never occur as isolated crystals surrounded by glass.
4) Their compositions vary greatly from that of the primary augite.
5) Furthermore, their spatial zonation patterns indicate that they grew from the olivine/liquid interface.

Our interpretation of these patterns (Fig. 7) is that each pyroxene nucleated at the olivine-liquid boundary in the zone ("the nucleus") which has the lowest Al_2O_3, TiO_2 and CaO contents and is closest in composition to the primary augite. They then grew both laterally along the olivine-liquid interface, and inward toward the center of the inclusions, with increasing Al_2O_3, TiO_2 and CaO contents (Cr_2O_3 zonation is more complex and will be discussed later in conjunction with the Cr-spinel).

It is clear, then, that the overall trends of CaO, TiO_2 and Na_2O vs. Al_2O_3 shown by the pyroxenes (Fig. 9) reflect crystallization beginning with a composition near that of the primary augite and progressing to higher Al_2O_3, TiO_2, CaO and Na_2O contents. Two observations support the hypothesis that the corresponding trends shown by glasses from all inclusions (Fig. 9) result primarily from crystallization of these pyroxenes. First, inclusions whose glasses have less than ≈19% Al_2O_3 show no pyroxene, which suggests that little pyroxene crystallized in them (so the chances of sampling it are low). Second, there is a positive correlation between the maximum Al_2O_3 contents of the pyroxenes and the Al_2O_3 contents of their coexisting glasses. Together, these observations indicate that there are positive correlations between amount of pyroxene crystallized in an inclusion and the Al_2O_3 content of its glass, and between the extent of a pyroxene's compositional evolution (that is, how far its compositions extend along the observed trends) and the Al_2O_3 content of its glass. The two pyroxene variables—volume and extent of compositional evolution—cannot be completely distinguished because of effects of unrepresentative sectioning. We will therefore refer to these two properties collectively as extent of pyroxene evolution. In our model, then, each point along one of the glass trends represents the average composition of the liquid after a certain degree of pyroxene evolution. Furthermore, the least aluminous glass

(LAG) can be taken as a good first-order approximation to the composition of the liquid before crystallization of any pyroxene.

We can test this model quantitatively by means of fractional crystallization calculations, using the following assumptions:1) Crystallization began with the composition of the least aluminous pyroxene (LAP), from a liquid represented by the LAG. Initial distribution coefficients are given by the ratios of concentrations in LAP/LAG: $D_{Ca} \approx 1$ to 1.2; $D_{Ti} \approx 0.4$ to 0.45; $D_{Na} \approx 0.08$; and $D_{Al} \approx 0.15$ to 0.20. With the exception of D_{Ti}, which is high, these values are similar to equilibrium distribution coefficients measured in basaltic systems at temperatures of ≈1150 to 1250°C (Grove and Bence, 1979; Longhi and Pan, 1989). 2) Crystallization ended with the composition of the most aluminous pyroxene (MAP), resulting in a residual liquid close to the composition of the most aluminous glass (MAG). Final distribution coefficients are given by concentrations in MAP/MAG: $D_{Ca} \approx 2.9$; $D_{Ti} \approx 4$; $D_{Na} \approx 0.1$ to 0.12; and $D_{Al} \approx 0.5$. These values are quite high relative to equilibrium values. The value for Al is within the range measured for augite by Grove and Bence (1979) at very high cooling rates (150–600°C/h) in the T range ≈ 1050 to 1100°C. The values for Ti and Ca, however, are much higher than those measured by Grove and Bence (1979) for these elements under such conditions (≈1 and ≈1.5–1.6, respectively). Initially, we assumed that the distribution coefficients varied (increased) linearly with degree of crystallization (relative to the initial volume).

Results of these calculations are shown in Figure 15. For the Na_2O-Al_2O_3 trends, good matches to both the pyroxenes and the glasses are obtained for 40 to 50% crystallization. For both the CaO-Al_2O_3 and TiO_2-Al_2O_3 trends, good matches to the glasses are obtained for similar degrees of crystallization. In both cases, however, the trends calculated for the pyroxenes are poor matches to those observed, having much steeper initial slopes, progressing to much higher CaO or TiO_2 contents, and showing turnovers in slope at high degrees of crystallization. Calculations made with more complex functions for the dependence of change in D on crystallization interval (logarithmic, exponential) did not produce qualitatively different results.

The success of these calculations in matching the observed pyroxene and glass trends for Na_2O and Al_2O_3, both of which behave incompatibly over the entire range of pyroxene compositions, demonstrates that our model is essentially correct. The failure of these calculations to match the observed CaO and TiO_2 variation in the pyroxenes can be accounted for by the fact that apparent D values for these elements greatly exceed unity. As discussed by Grove and Bence (1979), at high growth rates concentrations of elements that should be excluded from the pyroxene (e.g., Ti, Cr, Al) build up at the pyroxene/liquid interface and are incorporated into the rapidly growing crystal, with coupled substitution playing a major role. In addition, because Ca is a major element in the pyroxene structure, its concentration is crystallographically controlled. These effects cannot be described by normal partitioning models. It is clear that these pyroxenes formed at high growth rates under highly disequilibrium conditions.

This analysis of the pyroxene and glass trends allow us to conclude that, to first order, crystallization of pyroxene is responsible for the observed glass trends, and the LAG is a good estimate of the composition of the liquid before pyroxene crystallization. Therefore, although in the previous section we showed that olivine around all inclusions records cocrystallization of pyroxene, the ratio of olivine to pyroxene that was crystallizing during this interval (the final ≈5% of olivine crystallization) was very low. It is not necessary to adjust the

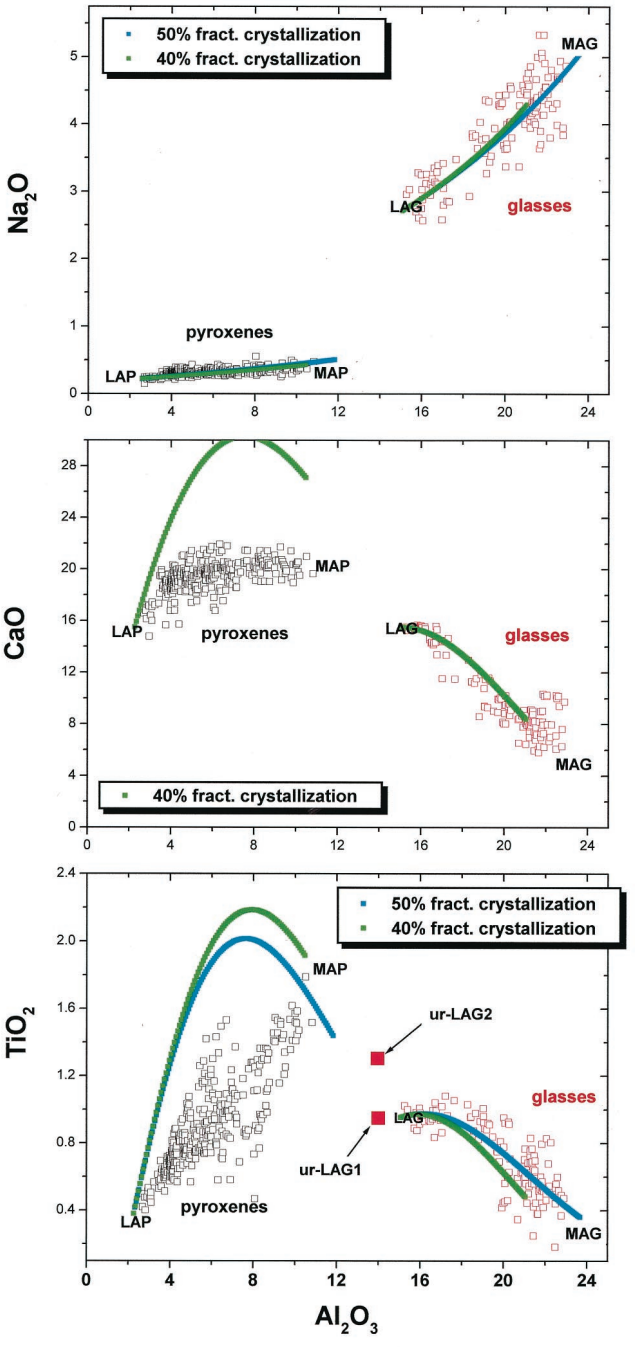

Fig. 15. Results of fractional crystallization calculations based on the assumption that the least aluminous pyroxene (LAP) coexisted with the least aluminous glass (LAG) and the most aluminous pyroxene (MAP) coexisted with the most aluminous glass (MAG). See text for details. Based on zonation of Cr in olivine around the LAG, glass trends have been extrapolated to give two estimates of the composition of the trapped liquid before crystallization of pyroxene (ur-LAG1 and ur-LAG2).

Table 8. Reconstruction of the composition of the Primary Trapped Liquid (PTL).

	LAG	ur-LAG1	ur-LAG1 +10%[a] FeO	ur-LAG2	ur-LAG2 +10%[a] FeO	PTL1[b]	PTL2[c]	PTLg[d]
SiO_2	57.5	58.6	53.3	56.2	51.1	47.8	46.6	46.5
TiO_2	0.98	0.99	0.90	1.27	1.15	0.6	0.8	0.5
Al_2O_3	16.3	14.6	13.3	14.8	13.4	8.9	9.3	8.3
Cr_2O_3	0.18	0.19	0.17	0.21	0.19	0.7[e]	0.7[e]	0.7[e]
FeO	3.1	3.2	12.0	3.2	12.0	15.9	15.6	14.6
MgO	2.7	2.8	2.5	2.9	2.6	13.5	13.0	19.0
MnO	0.23	0.23	0.21	0.23	0.21	0.7[e]	0.7[e]	0.7[e]
CaO	16.0	16.3	14.8	19.1	17.4	10.0	12.0	8.2
K_2O	0.04	0.04	0.04	0.04	0.04	0.03	0.02	0.02
Na_2O	3.0	3.1	2.8	2.1	1.9	1.9	1.3	1.5
Total	100.0	100.0	100.0	100.0	100.0	100.0	100.0	100.0
Fe/Mg	0.64	0.64	2.7	0.64	2.6	0.66	0.67	0.43
Ca/Al	0.90	1.01	1.01	1.17	1.17	1.02	1.18	0.90

[a] Before renormalization.
[b] 33 vol% olivine added, as described in text.
[c] 29 vol% olivine added, as described in text.
[d] Goodrich et al. (1999b); 50 vol.% olivine added.
[e] Adjusted after addition of olivine.

liquid composition for this small amount of olivine at this point in our reconstruction, because all olivine readdition will be considered in a later step.

However, the observation that some zonation of olivine is observed even around those inclusions containing the LAG, indicates that some pyroxene (not sampled in our sections) must have crystallized in these inclusions. Therefore, the glass trends must be extrapolated to obtain the true composition of the liquid before crystallization of pyroxene (ur-LAG). From the degree of Cr zonation around the LAG, we calculate maximum pyroxene crystallization of 10 to 15%, based on which we extrapolate the glass trends to an Al_2O_3 content of ≈14% (vs. ≈16% in the LAG). The fractional crystallization calculations suggest that the glass trends are close to flat at the beginning of crystallization (Fig. 15). If this is correct, the ur-LAG should have TiO_2, CaO, Na_2O (and SiO_2) contents similar to those of the LAG. We list this estimated composition, after renormalization, in Table 8 (ur-LAG1). It may be wise to also consider linear extrapolations of the glass trends. In this case the ur-LAG would have higher CaO and TiO_2 and lower Na_2O and SiO_2 contents than the LAG. We also list such an estimated composition (ur-LAG2) in Table 8. The most important difference between ur-LAG1 and ur-LAG2 is in Ca/Al ratio; that of ur-LAG2 is significantly higher.

7.1.3. Appearance of Cr-spinel and formation of metallic spherules

The Cr_2O_3-Al_2O_3 data for the pyroxenes (Fig. 9) show more scatter than those for other elements, and suggest a trend with a sudden reversal in slope from positive to negative. This trend is even more apparent in the zonation profiles for individual pyroxenes (Fig. 7), some of which show the reversal, and some of which have been sampled only after it. This reversal can be attributed to the appearance of Cr-spinel when Al_2O_3 in the pyroxenes reached ≈6%. The extremely low Cr_2O_3 contents (≈0.0–0.1%) of the glasses, and the low Cr contents of sulfides in the inclusions compared with primary interstitial sulfides (Table 4) further indicate that most of the Cr in the system has been sequestered in spinel.

Cr-spinel does not occur in the primary mineral assemblage of Hughes 009, nor of any ureilite except the unusual LEW 88774 (Warren and Kallemeyn, 1994; Prinz et al., 1994). Moreover, the Cr concentration of the primary olivine in Hughes 009 (again, as in all ureilites) is too high to have been in equilibrium with spinel. Such high Cr concentrations in olivine probably reflect the stabilization of Cr^{2+} in spinel-undersaturated melts at low fO_2 (Li et al., 1995; Hanson and Jones, 1998). The appearance of Cr-spinel in the inclusions can be attributed to a closed-system reaction involving reduction of FeO and simultaneous oxidation of Cr^{2+} to Cr^{3+}. As discussed by Li et al. (1995), in such a system cooling and fractional crystallization would eventually lead to saturation with Cr^{3+}-bearing spinel. If the system is closed, as it must have been in these inclusions, the oxygen needed to convert Cr^{2+} to Cr^{3+} must come from some other component. In this case, the obvious source is FeO:

$$FeO + 2Cr^{2+}O = Cr_2O_3 + Fe.$$

The Fe metal produced by this reaction joined whatever metal was already present (forming immiscible metal-sulfide liquids now represented by the spherules), and the Cr_2O_3 formed spinel. We can estimate the amount of spinel expected to form by this reaction. As calculated above, the Cr_2O_3 concentration of the primary trapped liquid was ≈0.7%; after fractional crystallization of olivine it may have risen to ≈1%. The above reaction could produce ≈2 wt.% (≈1 vol.%) of pure $FeCr_2O_4$ (chromite), which is consistent with observations (though we note that the spinel in the inclusions is not pure chromite). It would also result in loss of ≈1% FeO from the silicate melt—part of this to metal by reduction and part to the spinel. In our calculation of the composition of the PTL, then, we must consider this loss of FeO; this will be accomplished in a further

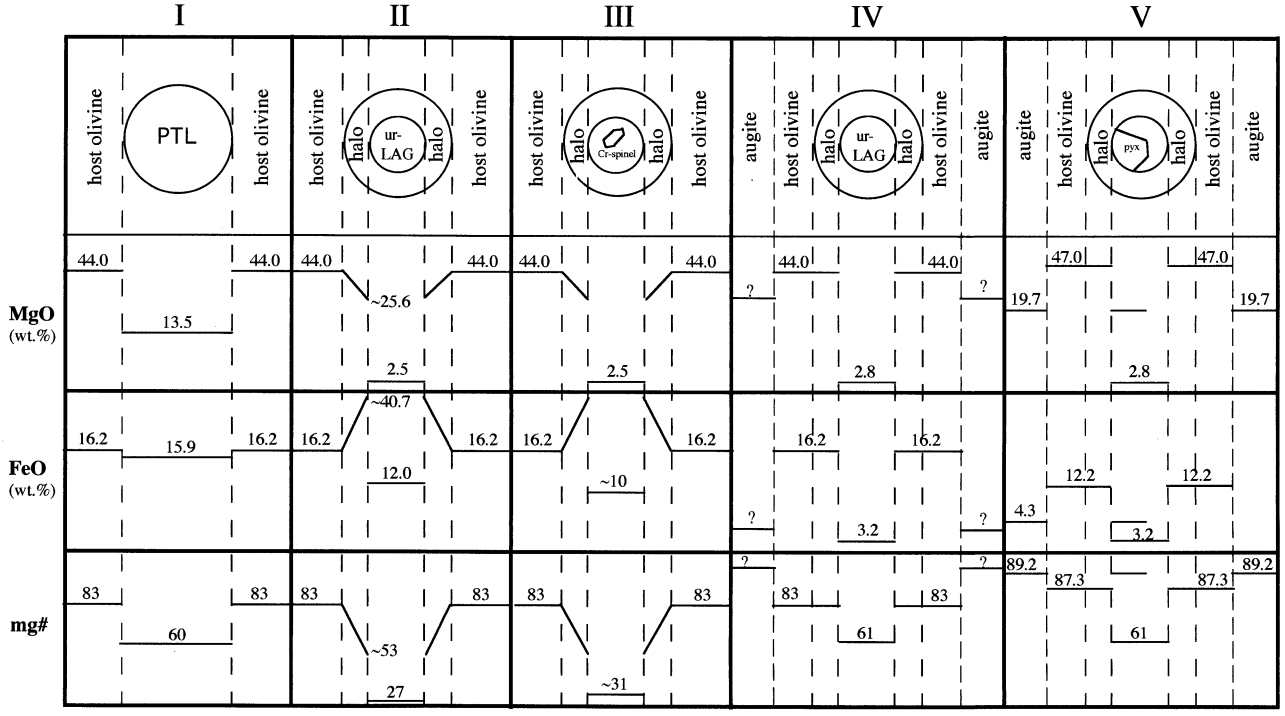

Fig. 16. Schematic illustration of the inferred evolution of FeO, MgO and *mg* for inclusions and primary silicates in Hughes 009, modelled after Figure 4a of Danyushevsky et al. (2000). See text for explanation.

discussion of FeO-loss. We must also restore the original Cr_2O_3 content of 0.7%; this is most easily accomplished in the final step of the reconstruction. Strictly speaking, we should also correct for loss of Al_2O_3 and MgO to spinel and loss of P_2O_5 to metal. However, these corrections would be minor and so are ignored.

7.1.4. Fe/Mg reequilibration and calculation of olivine component

There is evidence that all phases in the inclusions have exchanged Fe/Mg with their host: the halo olivine is homogeneous in Fe/Mg (0.146; *mg* 87.3) and identical to the host olivine; the pyroxenes are also relatively homogeneous in Fe/Mg (0.131 ± 0.008; *mg* 88.4) and are nearly identical to the primary augite (0.121; *mg* 89.2); and the glasses show only a small variation in Fe/Mg (0.64 ± 0.07; *mg* 61) which is not correlated with Al_2O_3 content. Reequilibration of Fe/Mg with the host is commonly observed in melt inclusions (e.g., Sobolev and Shimizu, 1993; Treiman, 1993; Danyushevsky et al., 2000; Gaetani and Watson, 2000) and can occur even when zonation of other elements (as in this case, Cr_2O_3 and CaO in the olivine and CaO, Al_2O_3, TiO_2, Na_2O and Cr_2O_3 in the pyroxene) is preserved, because Fe-Mg exchange is relatively fast.

In addition, there is evidence that the primary augite and olivine in Hughes 009 have reequilibrated Fe/Mg. The two-pyroxene equilibration T calculated by QUILF (Andersen et al., 1993) for the primary augite-orthopyroxene pair (based on Ca exchange) is 1250 ± 38°C. This is similar to pyroxene equilibration temperatures calculated for other ureilites (Takeda, 1987; Takeda et al., 1989; Chikami et al., 1997). However, the equilibration T calculated for the olivine-augite-orthopyroxene assemblage based on Fe/Mg exchange is 1066 ± 54°C. Furthermore, the equilibrium olivine composition calculated for the higher T is *mg* 83. This is precisely the composition with which the mean glass would have been in equilibrium ($K_D^{Fe/Mg}$ = 0.33). Therefore, it appears that the inclusions equilibrated Fe/Mg with their host olivine (*mg* 83) at high temperatures, and that the primary olivine and pyroxene later exchanged Fe/Mg only with each other.

Figure 16 (modelled after Fig. 4a of Danyushevsky et al., 2000) shows schematically the evolution of Fe/Mg ratios that we reconstruct for Hughes 009 by working backwards from the present situation. This situation is shown in Stage V: all pyroxenes (augite with *mg* ≈ 89 and orthopyroxene with *mg* ≈ 88) and all olivine (*mg* 87.3) record an equilibrium established among themselves at ≈1050°C, while the residual liquid in the inclusions (now represented by glass) has *mg* which is too low to be in equilibrium with them (we note that the *mg* ratios of the pyroxenes must have originally been somewhat higher than they are now, although this difference is not important for our model). Stage IV shows the inferred situation just before pyroxene-olivine reequilibration: the residual liquid in the inclusions and the olivine halos have completely equilibrated with the host olivine, whose composition of *mg* ≈ 83 still reflected high-T (1200–1250°C) conditions. This situation should be compared with stage II, which shows that originally the olivine halos which grew from the trapped melt most likely did so fractionally, with *mg* decreasing inward from the host value. As shown by Danyushevsky et al. (2000), reequilibration of the inclusions with the host (Stage IV) involves gain of MgO

and loss of FeO from the olivine halos and loss of FeO from the residual liquid, to bring the former to the host composition and the latter to equilibrium with it. If the composition of the host is known, then the original *mg* of the trapped liquid can be restored by a reverse fractional crystallization calculation such as that used by Sobolev and Shimizu (1993). However, because of the loss of FeO from the residual liquid during reequilibration, such a calculation will not yield the correct FeO and MgO contents for the PTL. An independent estimate of the original FeO content (or amount of FeO-loss from the residual liquid) is required.

In the case of Hughes 009, an estimate of FeO-loss from the residual liquid can be obtained from the following observation. Figure 17a shows the compositions of the glasses and pyroxenes projected from plagioclase in the system Ol-Pl-Wo-SiO_2. Since the glass compositions can be attributed primarily to crystallization of the pyroxenes, they should show a trend on this diagram that can be generated from the LAG by moving directly away from the pyroxenes. This is not the case. If, however, we add ≈10% FeO to their compositions, they move to a position that satisfies this requirement (Fig. 17a). This value reflects the total loss of FeO, including that which was incorporated into Cr-spinel (Stage III, Fig. 16). We note that Fe/Mn ratios of all phases in the inclusions reflect the same reequilibration processes as do Fe/Mg ratios (Fig. 9). This is not surprising, as the geochemical behavior of Mn is similar to that of Fe^{2+}, and it diffuses at similar rates. It is therefore likely that the residual liquid also suffered MnO-loss. To estimate the original MnO content of the PTL, we will simply require its Fe/Mn ratio to be equal to that of the primary olivine ($D^{Fe/Mn} \approx 1$).

Once we add 10% FeO to the estimated ur-LAG compositions (Table 8; columns 3 and 5), as shown in Stage II of Figure 16, we can perform the reverse fractional crystallization calculation (Sobolev and Shimizu, 1993), using the formulations of Ford et al. (1983) for D_{Mg} and D_{Fe}, and evolving back to *mg* 83. From this calculation we obtain simultaneously the amount of olivine crystallized from the trapped liquid and the primary composition of this liquid (Stage I, Fig. 16. The results are 40 wt.% (≈33 vol.%) and 36 wt.% (≈29 vol.%) olivine for ur-LAG1 and ur-LAG2, respectively, and the compositions PTL1 and PTL2 (Table 8; columns 6, 7; after final adjustment of Cr_2O_3 and MnO as described above). This indicates that our estimate from point-counting, of 50% plated-on olivine, is too high (even though this is the lowest value observed) because no inclusions have been sectioned representatively. PTL1 and PTL2 differ from the composition derived by Goodrich et al. (1999b) by adding 50 vol.% olivine (and evolving back to a primary olivine of *mg* 87) to the LAG (PTLg; Table 8, column 8) principally in having higher Fe/Mg and Ca/Al ratios. PTL1 and PTL2 are tholeiitic basalts, and PTLg is a picritic basalt (CIPW norm).

7.1.5. Quenching and late-stage reduction

After crystallization of pyroxene, the residual liquids were quenched to glass. TEM observations show that no nuclei of any other phases formed. The presence of typical effects of late C-reduction in Hughes 009 indicates that the primary magma contained carbon (though the compositionally limited extent of the reduction and the absence of carbon in the rock now indicates that it was probably less than in most ureilites, and was entirely consumed). Therefore, the trapped melts probably contained some carbon and may also have experienced late reduction of FeO. However, no correction is required for any FeO-loss due to this reaction, because all FeO-loss from the inclusions was considered collectively above. CO formed in this reaction may be dissolved in the glasses, or present as small fluid inclusions not yet observed. Alternatively, it may have been lost through fractures.

7.2. The Primary Trapped Liquid and Petrogenesis of Hughes 009

Figure 17 shows the compositions PTL1, PTL2 and PTLg projected in three subsystems of the system Ol-Wo-Pl-SiO_2. Examination of the compositions of the glasses and pyroxenes in the inclusions on these diagrams shows clearly that the crystallization sequence of the trapped liquid within the inclusions did not follow the equilibrium path. From the {Pl} projection (Fig. 17a) it can be seen that augite failed to nucleate at the point of olivine-augite co-saturation, and olivine "overcrystallized." The compositional path followed by the liquid was then determined almost solely by crystallization of augite rather than following the olivine-augite boundary curve. Furthermore, neither plagioclase (Fig. 17b,c) nor low-Ca pyroxene (Fig. 17a) nucleated as they should have when the liquid reached the augite—plagioclase or augite—low-Ca pyroxene boundaries (with the exception of the one inclusion in host crystal 2 which shows a small tip of orthopyroxene on skeletal augite).

The equilibrium crystallization sequences calculated by MAGPOX (Longhi, 1991) for all three estimated PTL compositions are shown in Figure 18. It is clear from these, as well as the phase diagrams (Fig. 17), that the PTL was saturated only with olivine. This conclusion allows us to address an issue that so far we have sidestepped—is Hughes 009 a cumulate or a residue? There can be no doubt that the inclusion-bearing olivine crystals were growing from a liquid when they trapped the inclusions. This does not, however, necessarily imply a cumulate origin for Hughes 009, because in a melting environment in which temperature is changing only slowly there can be material flux allowing some crystals to form as others melt. Nevertheless, the composition of this liquid cannot be reconciled with a residue model, because a melt in equilibrium with the residue from which it was derived should be saturated with all major phases present (e.g., Schiano and Bourdon, 1999; Schiano et al., 1998). Therefore, we conclude that Hughes 009 must be a cumulate. This is consistent with its Fe-Mn-Mg systematics, when compared to olivine-pigeonite ureilites (Fig. 2). Olivine in the latter has chondritic Mn/Mg ratios consistent with their being residues from low degrees of melting of chondritic material; olivine in Hughes 009 (like LEW 88774) has a distinctly higher Mn/Mg ratio that suggests the presence of a melt component (as demonstrated by Goodrich and Delaney [2000], low-degree [$< \approx 30\%$] melts of chondritic material have much higher Mn/Mg ratios than their precursors, while those of the residues are barely changed). Furthermore, since the PTL is saturated only with olivine, the composition of the Hughes 009 parent magma can differ from that of the PTL

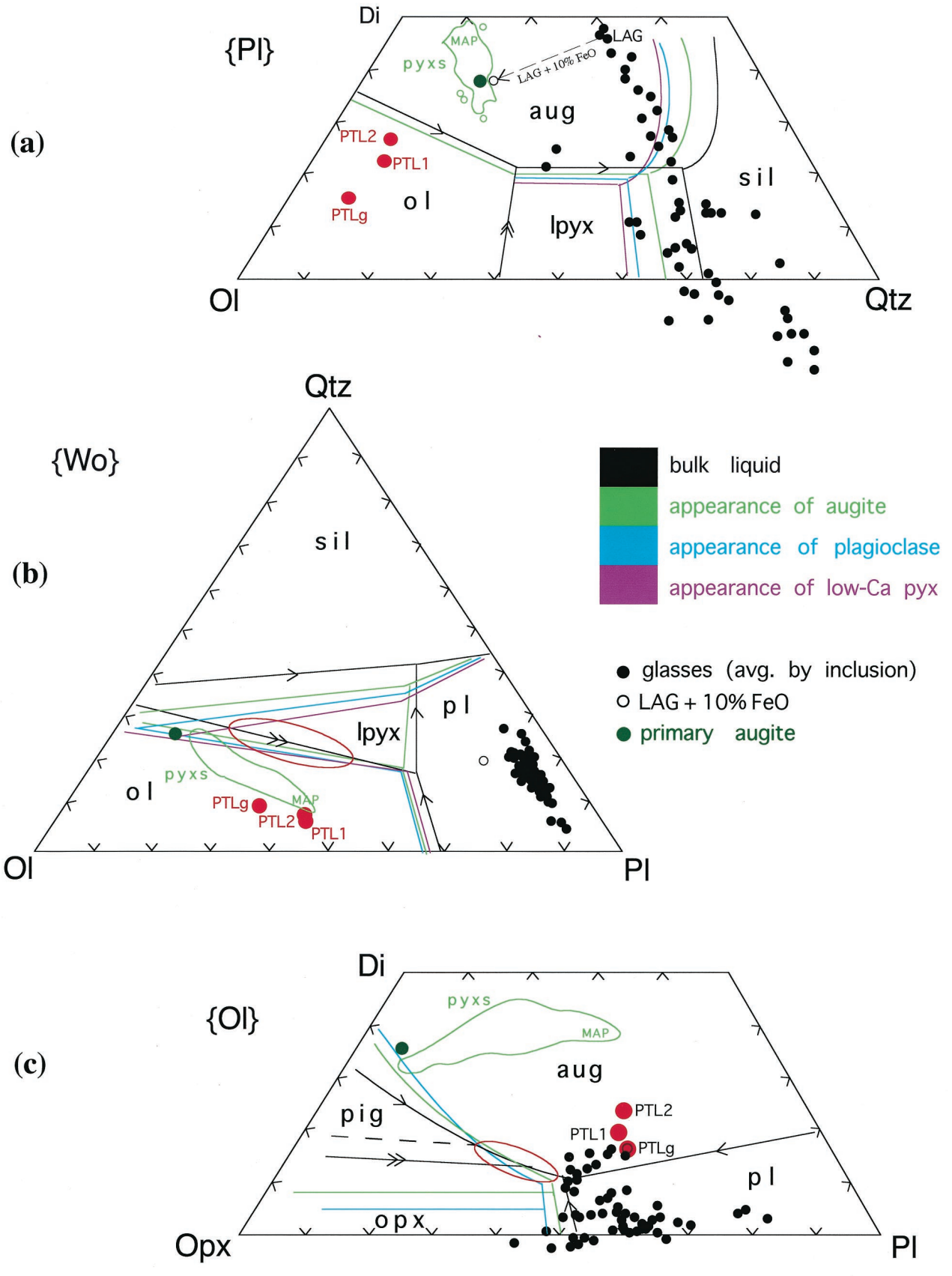
(a)
{Pl}
Di
Ol
Qtz
MAP
pyxs
LAG
LAG + 10% FeO
aug
PTL2
PTL1
PTLg
ol
lpyx
sil
(b)
{Wo}
Qtz
Ol
Pl
sil
lpyx
pl
ol
pyxs
PTLg
MAP
PTL2
PTL1
bulk liquid
appearance of augite
appearance of plagioclase
appearance of low-Ca pyx
glasses (avg. by inclusion)
LAG + 10% FeO
primary augite
(c)
{Ol}
Di
Opx
Pl
pyxs
MAP
aug
pig
PTL2
PTL1
PTLg
pl
opx

only in having a higher olivine component. Therefore it is appropriate to compare the crystallization sequence predicted for the PTL with the primary mineral assemblage of this ureilite.

The low-pressure crystallization sequences predicted for all three PTL compositions are similar (Fig. 18). Olivine is the liquidus phase. Augite appears after ≈23%, 18% or 40% (for PTL1, PTL2 and PTLg, respectively) crystallization. Plagioclase appears at ≈37%, 36% or 44% crystallization. Low-Ca pyroxene does not appear until 87%, 93% or 83% crystallization. In all cases, the low-Ca pyroxene is pigeonite rather than orthopyroxene. The final phase assemblage for all three compositions is dominated by olivine and plagioclase, with lesser augite and only a small amount of low-Ca pyroxene. Thus, neither the order of appearance of phases, nor the final assemblage predicted for these liquids is consistent with the bulk mineralogy of Hughes 009. Moreover, the temperatures calculated for the appearance of augite (≈1150–1190°C) are not consistent with the much higher two-pyroxene equilibration temperature (≈1250°C) of its primary augite-orthopyroxene assemblage. Such liquids could not produce an olivine-augite-orthopyroxene cumulate.

Magmas which could produce olivine-augite-orthopyroxene cumulates would plot in a region near the olivine-low-Ca pyroxene boundary in Figure 17b and the augite—orthopyroxene boundary in Figure 17c (red ellipses). Higher *mg* (as for PTLg) expands this region by expanding the range of compositions for which orthopyroxene, rather than pigeonite, is the stable low-Ca pyroxene. Such magmas would crystallize orthopyroxene before plagioclase (which would allow effective separation of olivine, augite and orthopyroxene). The principle adjustment that could be made to our PTL compositions to bring them into the range of such magmas is to increase their SiO_2 contents (Fig. 17b,c). For this reason, we specifically searched for overlooked reservoirs of SiO_2 in the inclusions. None were found.

It is important to note that the failure of the estimated PTLs to reproduce the bulk mineralogy of Hughes 009 does not depend on any of the points of our model which may be uncertain (e.g., the correct form of the glass trends, or the primary composition of the olivine), since all 3 of them show similar behavior. In addition, the SiO_2 content of PTLg was artificially elevated (we now believe, inappropriately) because early in our work we suspected that the low totals shown by the glasses were due to inaccurately low SiO_2 measurements. This illustrates that such adjustments to the SiO_2 content of the PTL as can be (even remotely) justified on the basis of our observations are inadequate to transform it into a melt that would be predicted to yield an olivine-augite-orthopyroxene cumulate.

It is possible that the conditions of the MAGPOX calculation for the crystallization sequence of the PTL are not appropriate for Hughes 009. One condition that might differ is pressure. We note that for basaltic compositions generally similar to the PTL, the field of orthopyroxene stability expands with increasing pressure so that at ≈9 to 13 Kb it appears before plagioclase. This observation should probably not be considered relevant, however, since such pressures are too high for asteroidal parent bodies. Another possibility, indicated by the low totals of the glass analyses, is that the PTL contained volatile elements not accounted for in our reconstruction, which could have an effect on its crystallization behavior (for example, CO, as discussed above). Experimental determination of the crystallization sequence of the PTL under a variety of conditions could be enlightening.

Nevertheless, the composition of the PTL may be indicative of complex magmatic processes in the petrogenesis of this ureilite. The major difference between the melt trapped in olivine in Hughes 009 and the melt which produced the bulk mineral assemblage of this ureilite is that the former evolved as a closed system, whereas the latter need not have. Although the number of olivine-augite-orthopyroxene ureilites is small compared with the number of olivine-pigeonite ureilites, they contain sufficient evidence to suggest a complex magmatic evolution not evident in the olivine-pigeonite ureilites. Figure 3, for example, shows that their augite (and to a lesser extent also orthopyroxene) compositions define trends consistent with magmatic evolution or magmatic mixing processes (whereas the olivine-pigeonite ureilites show no trends at all). Furthermore, 6 of the 9 olivine-augite-orthopyroxene ureilites have an overall poikilitic texture (sometimes referred to as “bimodal”) characteristic of heteradcumulates from terrestrial layered igneous complexes (Jackson, 1961; Wager and Brown, 1967), in which olivine and augite (sometimes showing typical equilibrated ureilite texture and grain size) are enclosed by large oikocrysts of orthopyroxene (Berkley et al., 1985; Berkley, 1990; Goodrich, 1986; Goodrich, 1999b; Takeda et al., 1989; Weber and Bischoff, 1998). Unequivocal evidence that this is a reaction texture is found in LEW 88774, in which augite remnants in the orthopyroxene oikocryst preserve optical continuity (Goodrich, 1999b). Mixing of an orthopyroxene-saturated magma with an olivine-augite (±liquid) assemblage could produce this texture. Since addition of an orthopyroxene-saturated liquid would have the same effect as simple addition of SiO_2 to the PTL in Hughes 009 (Fig. 17), it is conceivable that this ureilite shows another textural manifestation of the magmatic mixing process evident in the bimodal olivine-augite-orthopyroxene ureilites. This suggestion is, in fact, consis-

Fig. 17. Projections from plagioclase (a), wollastonite (b) and olivine (c) in the system olivine-plagioclase-wollastonite-quartz, showing three estimates of the composition of the primary trapped liquid (PTL). In all three projections, low-pressure phase boundaries (calculated with MAGPOX) appropriate for the compositions PTL1 and PTL2 are shown, color coded to indicate their locations at the time of appearance of various phases. In the {Ol} projection, the orthopyroxene-pigeonite boundary for the bulk composition of PTLg is also shown (dashed black curve). Average compositions of glasses and fields for all pyroxene compositions (green outlined areas, with position of most aluminous pyroxene [MAP] indicated) in inclusions are also shown. Position of least aluminous glass (LAG) + 10% FeO (Fe-loss, as discussed in text) is shown in all three projections. Note that in our interpretaion, all glasses were originally similarly displaced from their present positions. Red ellipses in the {Wo} and {Ol} projections surround bulk compositions that might give rise to olivine-augite-orthopyroxene cumulates. See text for discussion. Projection equations in terms of oxygen units (Longhi, 1991).

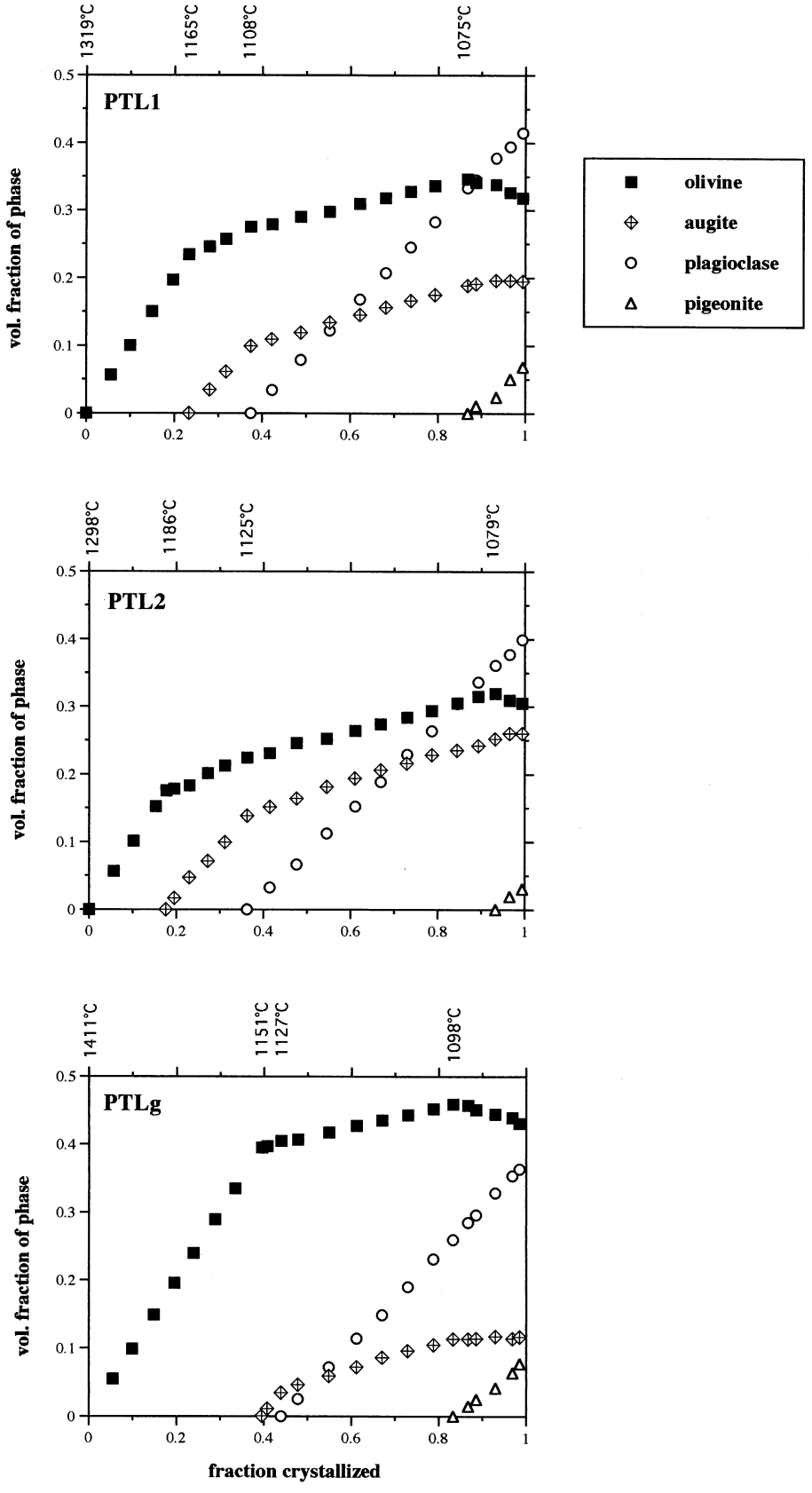

Fig. 18. Low-pressure equilibrium crystallization sequences, calculated with MAGPOX (Longhi, 1991), for three estimated PTL compositions. All show similar behavior, and produce final assemblages dominated by olivine and plagioclase, with lesser augite and small amounts of pigeonite.

tent with observed poikilitic relationships in Hughes 009 (small inclusions of olivine and augite in orthopyroxene).

If the PTL in Hughes 009 represents a primary ureilitic magma, two of its properties may be particularly significant with regard to the chemical composition and igneous evolution of the ureilite parent body (although some properties of ureilites suggest multiple parent bodies, the similar cooling and late-stage reduction histories shown by all ureilites [Mittlefehldt et al., 1998] are more consistent with a single body). First, its Ca/Al ratio is superchondritic (for PTL1, Ca/Al = 1.4 × CI), consistent with the conclusions of Goodrich et al. (1987) and Goodrich (1999a) that regardless of whether ureilites are cumulates or residues, they require precursor materials with superchondritic Ca/Al. Second, it is predicted to crystallize a significant amount of plagioclase, which suggests that plagioclase-rich rocks must have formed on the ureilite parent body (plagioclase is completely absent in monomict ureilites, and occurs in polymict ureilites only as a minor component). Thus, the discovery of melt inclusions in Hughes 009 further encourages the hope that the olivine-augite-orthopyroxene ureilites hold clues to ureilite petrogenesis that may not be present in the olivine-pigeonite ureilites.

7.3. Shock and Late-Stage Cooling History

Several lines of evidence suggest that Hughes 009 experienced only mild shock. Olivine shows only weak undulatory optical extinction, fracturing is irregular, and no planar defect textures are present. Mechanical polysynthetic twinning in augite is present at the optical but not the electron optical scale, and the twin frequency, as estimated along a*, is lower than observed in FRO 90054 (on average every 5×10^5 Å in Hughes 009 vs 5×10^2 Å in FRO 90054). The clinopyroxene lamellae within orthopyroxene, which can be interpreted as evidence that some shock occured (Takeda et al., 1989), are not widespread. The TEM analysis of opx1 showed the presence of the same (100) clinopyroxene lamellae with almost the same density as observed in the average samples. The presence of mechanical twinning, the lack of planar defect features in olivine and the lack of shock-induced glass places Hughes 009 at the S2 level of shock (Stöffler et al., 1991), and suggests a peak pressure of 5 to 10 GPa. The observed brecciation and fracturing clearly occurred after the shock event that induced twinning in pyroxenes, as shown in Figure 4d where twinning in augite is disrupted by in situ brecciation As discussed by Goodrich (1998), this texture most likely originated in the regime of brittle rather than plastic deformation (Bischoff and Stöffler, 1992), and involved heating sufficient to melt and redistribute only metal.

Combined TEM and single crystal data indicate fast cooling for Hughes 009. In Figure 12 the intracrystalline Fe^{2+}-Mg partitioning obtained for the orthopyroxene is compared with previous determinations on achondrites. It appears that the two ureilites for which cation partitioning in orthopyroxene has been determined—Hughes 009 (this work) and FRO 90054 (Tribaudino et al., 1997)—are the most disordered. Degree of the Fe^{2+}-Mg disorder is related to cooling rate (Ganguly, 1982; Ganguly et al., 1994) and therefore to the size of the cooling body. These results suggest fast cooling for ureilites. The lack of exsolution lamellae in augite, despite its relatively low Ca-content, further indicates that cooling was fast enough to inhibit exsolution, as observed only in fine-grained volcanic rocks. On the other hand, the cooling was not as fast as quenching of synthetic runs (hundreds of degrees per minute). In an investigation of synthetic samples along the join diopside-enstatite Tribaudino (2000) found mottled, non-periodic textures like those observed in most of the Hughes 009 clinopyroxene only in samples poorer in Ca than 0.7 apfu (atoms per formula unit) The occurrence of periodic and non-periodic mottled textures in this sample, which has a composition close to the Di-En join and a Ca content higher than 0.7 apfu, indicates that cooling was enough slower than that of the synthetic runs to permit formation of non-periodic textures.

A quantitative estimate of cooling rate for Hughes 009 can be obtained from Fe^{2+}-Mg intracrystalline cation partioning, according to the procedure outlined in Ganguly (1982). This procedure uses the Mueller chemical rate theoretical model (Mueller, 1967; Mueller, 1969) and an asymptotic cooling model ($1/T = 1/T_0 + \eta t$, where T_0 is the initial time and η is a cooling time constant with the dimension $K^{-1}t^{-1}$). The thermodynamic equilibrium calibration of k_D vs 1/T for intracrystalline partitioning was taken from Stimpfl et al. (1999) ($\ln k_D = -2854/T + 0.603$), and the kinetic constants of Ganguly and Tazzoli (1994) were used. The cooling rate thus calculated is 7(±5)°C/h ($\eta = 0.076$ K/yr) at the closure T of 630°C. This result is in agreement with the estimate of Mori and Takeda (1983) for ureilite Y 74130, based on the wavelength of spinodal decomposition in augite (3–20°C/h between 1250 and 800°C), and with that of Toyoda et al. (1986) for ureilite PCA 82506 based on reverse zoning profiles in olivine (10–15°C/h). Incidentally, the wavelength for spinodal decomposition found for augite in this work is lower than that found by Mori and Takeda (1983) ($\lambda \approx 130$ vs 190Å). If these two augites were of the same composition, a faster cooling rate would be indicated for Hughes 009. However, as discussed in Tribaudino et al. (1997), the kinetics of spinodal decomposition is affected by composition. The spinodal decomposition features observed in clinopyroxene in Hughes 009 are probably due to its more Ca-rich composition compared to the Y 74130 augite (≈0.74 vs ≈0.63 Ca apfu), rather than to faster cooling.

7.4. Overall Temperature-Cooling History of Hughes 009

The liquidus temperatures of ≈1320°C and 1300°C calculated by MAGPOX for PTL1 and PTL2, respectively, correspond to the time of trapping of the inclusions. The fact that melts were trapped during this period indicates that it was one of relatively rapid growth, but since rapid cooling is not the only condition that can lead to rapid growth and trapping of melts (Roedder, 1984), we cannot conclude that this was a period of rapid cooling. The reequilibration temperature of ≈1050°C calculated for olivine-augite-orthopyroxene Fe/Mg exchange suggests a period of slow cooling at lower T, during which the high degree of heterogeneity, the large grain sizes, and the equilibrated texture of the primary phases were established. It is not easy to establish when the pyroxenes in the inclusions crystallized, because their nucleation was clearly delayed. Their highly disequilibrium compositions, indicating extremely fast growth rates, are not, however, necessarily due to rapid cooling, but more likely result from a high degree of

supersaturation. In any case, they must have existed during the inferred period of slow cooling, since their Fe/Mg ratios are equilibrated.

This period of slow cooling must have been followed by a period of extremely rapid cooling, as evidenced by Fe^{2+}-Mg intracrystalline partitioning in the orthopyroxene, the lack of exsolution lamellae in the augite, and the lack of nuclei in the glasses in the inclusions. Our estimated cooling rate of 7 ± 5°C/h at 630°C is in agreement with evidence for extremely fast late cooling histories for other ureilites, and consistent with the interpretation that all ureilites have been excavated by impact (Mittlefehldt et al., 1998 and references therein). This event, being accompanied by a drop in pressure, led to late-stage carbon reduction reactions, as seen in all ureiltes, and to shock features. Hughes 009 appears to have experienced two distinguishable (though not necessarily widely separated in time) shock events: the first at peak pressures of 5 to 10 GPa, resulting in mechanical polysynthetic twinning in orthopyroxene and mild undulatory extinction in olivine; and the second, at lower pressures, resulting only in brecciation and redistribution of metal. We can be grateful to the overall low-shock level seen by this ureilite for preserving the melt inclusions in olivine.

Acknowledgments—We especially thank Marty Prinz for calling our attention to Hughes 009 and for providing samples. We also thank T. Grove, E. Jagoutz, J. Longhi, A. V. Sobolev, R. Strebel, A. Treiman, R. Zartmann and J. Zipfel for helpful discussions; B. Hoffman for providing samples; and B. Schulz-Dobrick, E. Macsenaere-Riester, K. Kadisch and P. Guerriero for assistance with EMPA and SEM. Cyrena Goodrich would like to thank Jack Berkley for his never-ending enthusiasm and support. We thank G. J. Taylor, J. Longhi, Y. Ikeda and H. Palme for their careful reviews and constructive comments. This work was partly supported by CNR, PNRA and MURST grants.

Associate editor: H. Palme

REFERENCES

Anderson A. T., Jr. (1974) Evidence for a picritic, volatile-rich magma beneath Mt. Shasta, California. *J. Petrol.* **15,** 243–267.

Andersen D. J., Lindsley D. H., and Davidson P. M. (1993) QUILF: A PASCAL program to assess equilibria among Fe-Mg-Mn-Ti oxides, pyroxenes, olivine, and quartz. *Comp. Geosci.* **19,** 1333–1350.

Baba T., Takeda H., and Saiki K. (1993) Mineralogy of three Euromet ureilites including an orthopyroxene-augite achondrite. *Meteoritics* **28,** 319. (abstr.).

Berkley J. L. (1990) Petrology of newly recovered orthopyroxene-bearing Antarctic ureilites: A new ureilite type? *Lunar Planet. Sci.* **21,** 69–70. (abstr.).

Berkley J. L., Taylor G. J., Keil K, Harlow G. E., and Prinz M. (1980) The nature and origin of ureilites. *Geochim. Cosmochim. Acta* **44,** 1579–1597.

Berkley J. L., Goodrich C. A., and Keil K. (1985) The unique ureilite, ALHA82106–82130: Evidence for progressive reduction during ureilite magmatic differentiation. *Meteoritics* **20,** 607–608.

Bischoff A. and Stoeffler D. (1992) Shock metamorphism as a fundamental process in the evolution of planetary bodies: Informations from meteorites. *Eur. J. Mineral.* **4,** 705–755.

Boynton W. V., Starzyk P. M., and Schmitt R. A. (1976) Chemical evidence for the genesis of the ureilites, the achondrite Chassigny and the nakhlites. *Geochim. Cosmochim. Acta* **40,** 1439–1447.

Brearley A. J. and Jones R. H. (1998) Chondritic meteorites. In *Planetary Materials* (ed. J. J. Papike). Mineralogical Society of America. *Rev. Mineral.* **36,** 370 pp.

Buseck P. R., Nord G. L., and Veblen D. R. (1980) Subsolidus phenomena in pyroxenes. In *Pyroxenes* (ed. C. T. Prewitt). Mineralogical Society of America. *Rev. Mineral.* **7,** 117–211.

Chikami J., Mikouchi T., and Miyamoto M. (1997) Mineralogy and cooling history of the calcium-aluminum-chromium enriched ureilite, Lewis Cliff 88774. *Meteoritics Planet. Sci.* **32,** 343–348.

Clayton R. N and Mayeda T. K. (1988) Formation of ureilites by nebular processes. *Geochim. Cosmochim. Acta* **52,** 1313–1318.

Clayton R. N. and Mayeda T. K. (1996) Oxygen isotope studies of achondrites. *Geochim. Cosmochim. Acta* **60,** 1999–2017.

Clocchiatti R. and Massare D. (1985) Experimental crystal growth in glass inclusions: The possibilities and limits of the method. *Contrib. Mineral. Petrol.* **89,** 193–204.

Danyushevsky L. V., Della-Pasqua F. N., and Sokolev S. (2000) Re-equilibration of melt inclusions trapped by magnesian olivine phenocrysts from subduction-related magmas: Petrological implications. *Contrib. Mineral. Petrol.* **138,** 68–83.

Donaldson C. H. and Brown R. W. (1977) Refractory megacrysts and magnesium-rich melt inclusions within spinel in oceanic tholeiites: Indicators of magma mixing and parental magma composition. *Earth Planet. Sci. Lett.* **37,** 81–89.

Fioretti A. M. and Molin G. (1996) Petrography and mineralogy of FRO 93008 ureilite: Evidence for pairing with FRO 90054 ureilite. *Meteoritics Planet. Sci. Suppl.* **31** (abstr. A43).

Fioretti A. M. and Molin G. (1998) FRO95028: A new low-shock ureilite close to ALHA78019. *Meteoritics Planet. Sci. Suppl.* **33** (abstr. A47).

Fioretti A. M., Molin G., Brandstätter F., and Kurat G. (1996) Schreibersite, metal and troilite in ureilites FRO 90054 and FRO 93008. *Meteoritics Planet. Sci. Suppl.* **31** (abstr. A44).

Floran R. J., Prinz M., Hlava P. F., Keil K, Nehru C. E., and Hinthorne J. R. (1978) The Chasssigny meteorite: A cumulate dunite with hydrous amphibole-bearing melt inclusions. *Geochim. Cosmochim. Acta* **42,** 1213–1229.

Ford C. E., Russell D. G., Craven J. A., and Fisk, M. R. (1983) Olivine-liquid equilibria: Temperature, pressure and compositional dependence of the crystal/liquid cation partition coefficients for Mg, Fe^{2+}, Ca and Mn. *J. Petrol.* **24,** 256–265.

Gaetani G. and Watson B. (2000). Open system behavior of olivine-hosted melt inclusions. *Earth Planet. Sci. Lett.* **183,** 27–41.

Ganguly J. (1982) Mg-Fe order-disorder in ferromagnesian silicates: II. Thermodynamics, kinetics and geological applications. In *Advances in Physical Geochemistry 2* (ed. S. K. Saxena). 353 pp. Springer-Verlag, New York.

Ganguly J. and Tazzoli V. (1994) Fe^{2+}-Mg interdiffusion in orthopyroxene: Retrieval from the data on intracrystalline exchange reaction. *Am. Mineral.* **79,** 930–937.

Ganguly J., Yang H., and Ghose S. (1994) Thermal history of mesosiderites: Constraints from compositional zoning and Fe-Mg ordering in orthopyroxenes. *Geochim. Cosmochim. Acta* **58,** 2711–2723.

Goodrich C. A. (1986) Y 74130: A ureilite with cumulus augite. *Meteoritics* **21** (abstr. 373–374).

Goodrich C. A. (1992) Ureilites: A critical review. *Meteoritics.* **27,** 327–352.

Goodrich C. A. (1998) A ureilite (Hughes 009) with an unusual shock texture: Implications for the origin of metal in ureilites? *Lunar Planet. Sci.* **29** (abstr. 1123).

Goodrich C. A. (1999a) Are ureilites residues from partial melting of chondritic material? The answer from MAGPOX. *Meteoritics Planet. Sci.* **34,** 109–119.

Goodrich C. A. (1999b) A primary silicate mineral/melt reaction texture in ureilite Lewis Cliff 88774. *Meteoritics Planet. Sci.* **34,** A44–A45. (abstr.).

Goodrich C. A. and Berkley J. L. (1986) Primary magmatic carbon in ureilites: Evidence from cohenite-bearing spherules. *Geochim. Cosmochim. Acta* **50,** 681–691.

Goodrich C. A. and Delaney J. S. (2000) Fe/Mg-Fe/Mn relations of meteorites and primary heterogeneity of primitive achondrite parent bodies. *Geochim. Cosmochim. Acta.* **64,** 149–160.

Goodrich C. A., Jones J. H., and Berkley J. L. (1987) Origin and evolution of the ureilite parent magmas: multi-stage igneous activity on a large parent body? *Geochim. Cosmochim. Acta* **51,** 2255–2273.

Goodrich C. A., Fioretti A. M., Molin G., and Tribaudino M. (1999a)

Primary trapped melt inclusions in olivine in a ureilite—I. *Description. Lunar Planet. Sci.* **30** (abstr. 1026).

Goodrich C. A., Fioretti A. M., Molin G., Zipfel J., and Tribaudino M. (1999b) Primary trapped melt inclusions in olivine in a ureilite—II. Reconstruction of liquid composition and implications. *Lunar Planet. Sci.* **30** (abstr. 1027).

Grove T. J. (1982) Use of exsolution lamellae in lunar clinopyroxenes as cooling rate speedometers: an experimental calibration. *Am. Mineral.* **67,** 251–268.

Grove T. L. and Bence A. E. (1979) Crystallization kinetics in a multiply saturated basalt magma: An experimental study of Luna 24 ferrobasalt. *Proc. Lunar Planet. Sci. Conf.* **10,** 439–478.

Grove T. L, Kinzler R. J., and Bryan W. B. (1990) Natural and experimental phase relations of lavas from Serocki Volcano. In *Proc. Ocean Drilling Program Sci. Results 106/109.* (eds. Detrick R., Honnorez J. Bryan W. B., Juteau T., et al.) pp. 9–17. College Station, TX.

Hanson B. and Jones J. H. (1998) The systematics of Cr^{3+} and Cr^{2+} partitioning between olivine and liquid in the presence of spinel. *Am. Mineral.* **83,** 669–684.

Harvey P. R. and McSween H. Y., Jr. (1992) The parent magma of the nakhlite meteorites: Clues from melt inclusions. *Earth Planet. Sci. Lett.* **111,** 467–482.

Ibers J. A. and Hamilton W. C., Eds. (1974) *International Tables for X-Ray Crystallography 4.* Kynoch Press, Birmingham, U.K. pp. 99–101.

Jackson E. D. (1961) Primary textures and mineral associations in the ultramafic zone of the Stillwater Complex, Montana. *Geol. Survey Professional Paper* **358,** US Gov. Printing Office, Washington, D.C. 106 pp.

Johnson M. C., Rutherford M. J., and Hess P. C. (1991) Chassigny petrogenesis: Melt compositions, intensive parameters, and water contents of Martian (?) magmas. *Geochim. Cosmochim. Acta* **55,** 349–366.

Kallemeyn G. W. and Warren P. H. (1994) Geochemistry of LEW88774 and two other unusual ureilites. *Lunar Planet. Sci.* **25,** 663–664. (abstr.).

Li J-P., O'Neil H. St C., and Seifert F. (1995) Subsolidus phase relations in the system MgO-SiO_2-Cr-O in equilibrium with metallic Cr, and their significance for the petrochemistry of chromium. *J. Petrol.* **36,** 107–132.

Longhi J. (1991) Comparative liquidus equilibria of hypersthene-normative basalts at low pressure. *Am. Mineral.* **76,** 785–800.

Longhi J. and Pan V. (1989) The parent magmas of the SNC meteorites. *Proc. Lunar Planet. Sci. Conf.* **19,** 451–464.

Mittlefehldt D. W., McCoy T. M., Goodrich C. A., and Kracher A. (1998) Non-chondritic meteoritics from asteroidal bodies. In *Planetary Materials* (ed. J. Papike). Mineralogical Society of America. *Rev. Mineral.* **36,** 170 pp.

Mori H. and Takeda H. (1983) An electron petrographic study of ureilite pyroxenes. *Meteoritics* **18,** 358–359. (abstr.).

Mueller R. F. (1967) Model for order-disorder kinetics in certain quasi binary crystals of continuously variable composition. *J. Phys. Chem. Solids* **28,** 2239–2243.

Mueller R. F. (1969) Kinetics and thermodynamics of intracrystalline distribution. *Mineral. Soc. Am. Spec. Paper* **2,** 83–93.

Nord G. L. and McCallister R. H. (1979) Kinetics and mechanism of decomposition in $Wo_{25}En_{31}Fs_{44}$ clinopyroxene. *Geological Society of America, Abstracts with Programs,* **11** (abstr. 488).

Pasqual D., Molin G., and Tribaudino M. (2000). Single-crystal thermometric calibration of Fe-Mg order-disorder in pigeonites. *Am. Mineral.* **85,** 953–962.

Price R. C., Kennedy A. K., Riggs-Sneeringer M., and Frey F. A. (1986) Geochemistry of basalts from the Indian Ocean triple junction: Implications for the generation and evolution of Indian Ocean ridge basalts. *Earth Planet. Sci. Lett.* **78,** 379–396.

Prinz M., Weisberg M. K., and Nehru C. E. (1994) LEW 88774: A new type of Cr-rich ureilite. *Lunar Planet. Sci.* **25,** 1107–1108. (abstr.).

Roedder E. (1976) Petrologic data from experimental studies on crystallized silicate melt and other inclusions in lunar and Hawaiian olivine. *Am. Mineral.* **61,** 684–690.

Roedder E. (1979) Origin and significance of magmatic inclusions. *Bull. Mineral.* **102,** 487–510.

Roedder E. (1984) Fluid Inclusions. Mineralogical Society of America. *Rev. Mineralogy* **2,** 12–26.

Roedder E. and Weiblen P. W. (1970) Lunar petrology of silicate melt inclusions, Apollo 11 rocks. *Proc. Apollo 11 Lunar Sci. Conf.* **1,** 801–837.

Roedder E. and Weiblen P. W. (1971) Petrology of silicate melt inclusions, Apollo 11 and Apollo 12 and terrestrial equivalents. *Proc. 2nd Lunar Sci. Conf.* **1,** 507–528.

Rossi G., Oberti R., Dalnegro A., Molin G. M., and Mellini M. (1987) Residual electron density at the M2 site in C2/c clinopyroxene: relationships with bulk chemistry and subsolidus evolution. *Phys. Chem. Miner.* **14,** 514–520.

Rutherford M. J. and Devine J. D. (1988) The May 18, 1980, eruption of Mount St. Helens 3. Stability and chemistry of amphibole in the magma chamber. *J. Geophys. Res.* **93, no. 10,** 11949–11959.

Schiano P. and Bourdon B. (1999) On the preservation of mantle information in ultramafic nodules: Glass inclusions within minerals versus interstitial glasses. *Earth Planet. Sci. Lett.* **169,** 173–188.

Schiano P., Bourdon B., Clocchiatti R., Massare D., Varela M. E., and Bottinga Y. (1998) Low-degree partial melting trends recorded in upper mantle minerals. *Earth Planet. Sci. Lett.* **160,** 537–550.

Schreiber H. D. and Haskin L. A. (1976) Chromium in basalts: experimental determination of redox states and partitioning among synthetic silicate phases. *Proc. Lunar Sci. Conf.* **7,** 1221–1259.

Scott E. R. D., Taylor G. J., and Keil K. (1993) Origin of ureilite meteorites and implications for planetary accretion. *Geophys. Res. Lett.* **20,** 415–418.

Sheldrick G. M. (1997) Shelxl-97. Program for crystal structure refinement. Goettingen University, Germany.

Sinton C. W., Christie D. M., Coombs V. L., Nielsen R. L. and Fisk M. R. (1993) Near primary melt inclusions in anorthite phenocrysts from the Galapogos Platform. *Earth Planet. Sci. Lett.* **119,** 527–537.

Sobolev A. V. (1996) Melt inclusions in minerals as a source of principle petrological information. *Petrology* **4,** 209–220. Translated from *Petrologiya.* **4,** 228–239.

Sobolev A. V. and Danyushevsky L. V. (1994) Petrology and geochemistry of boninites from the north termination of the Tonga trench: Constraints on the generation conditions of primary high-Ca boninite magmas. *J. Petrol.* **35,** 1183–1211.

Sobolev V. S. and Kostyuk. (1975) Magmatic crystallization based on a study of melt inclusions. Nauka Press. Novosibirsk. Translated in part in *Proc. COFFI* **9,** 182–253.

Sobolev A. V.and Shimuzu N. (1993) Ultra-depleted primary melt included in an olivine from the Mid-Atlantic Ridge. *Nature* **363,** 151–154.

Sobolev A. V., Dmitriev L. V., Barsukov V. L., Nevsorov V. N., and Slutsky A. B. (1980) The formation conditions of the high-magnesium olivines from the monomineralic fraction of Luna 24 regolith. *Proc. Lunar Planet. Sci. Conf.* **11,** 105–116.

Stimpfl M., Ganguly J., and Molin G. (1999) Fe^{2+}-Mg order-disorder in orthopyroxene: equilibrium fractionation between the octahedral sites and thermodynamic analysis. *Contrib. Mineral. Petrol.* **136,** 297–309.

Stöffler D., Keil K., and Scott E.R.D. (1991) Shock metamorphism of ordinary chondrites. *Geochim. Cosmochim. Acta* **55,** 3845–3867.

Takeda H. (1987) Mineralogy of Antarctic ureilites and a working hypothesis for their origin and evolution. *Earth Planet. Sci. Lett.* **81,** 358–370.

Takeda H. (1989) Mineralogy of coexisting pyroxenes in magnesian ureilites and their formation conditions. *Earth Planet. Sci. Lett.* **93,** 181–194.

Takeda H., Mori H., and Ogata H. (1989) Mineralogy of augite-bearing ureilites and the origin of their chemical trends. *Meteoritics* **24,** 73–81.

Toyoda H., Haga N., Tachikawa O., Takeda H. and Ishii T. (1986) Thermal history of ureilite, Pecora Escarpment 82506 deduced from cation distribution and diffusion profile of minerals. *Proceedings of. 10th Symposium on Antarctic Meteorites* 206– 221.

Treiman A. (1992) Foundation of forensic meteoritics. *Meteoritics* **27,** 298–299. (abstr.).

Treiman A. (1993) The parent magma of the Nakhla (SNC) meteorite, inferred from magmatic inclusions. *Geochim. Cosmochim. Acta* **57,** 4753–4767.

Treiman A. and Berkley J. L. (1994) Igneous petrology of the new ureilites Nova 001 and Nullarbor 010. *Meteoritics* **29,** 843–848.

Tribaudino M. (2000). A transmission electron microscope investigation on the C2/c -$P2_1$/c phase transition in clinopyroxenes along the diopside-enstatite ($CaMgSi_2O_6$-$Mg_2Si_2O_6$) join. *Am. Mineral.* **85,** 707–715.

Tribaudino M., Fioretti A.M., Martignago F., and Molin G. (1997) Transmission electron microscope texture and crystal chemistry of coexisting ortho- and clinopyroxene in the Antarctic ureilite Frontier Mountain 90054: Implications for thermal history. *Meteoritics Planet. Sci.* **32,** 671–678.

Wager L. R. and Brown G. M. (1967) Layered Igneous Rocks. Oliver and Boyd.

Warren P. H. and Kallemeyn G. K. (1989) Geochemistry of polymict ureilite EET83309, and a partially-disruptive impact model for ureilite origin. *Meteoritics* **24,** 233–246.

Warren P. H. and Kallemeyn G. K. (1992) Explosive volcanism and the graphite-oxygen fugacity buffer on the parent asteroid(s) of the ureilite meteorites. *Icarus.* **100,** 110–126.

Warren P. H. and Kallemeyn G. K. (1994) Petrology of LEW88774: An extremely chromium-rich ureilite. *Lunar Planet. Sci.* **25** (abstr. 1465–1466).

Weber I. and Bischoff A. (1998) Mineralogy and chemistry of the ureilites Hammadah Al Hamra 064 and Jalanash. *Lunar Planet. Sci.* **29** (abstr. 1365).

Wlotzka F. (1994) The Meteoritical Bulletin, No. 77, 1994 November. *Meteoritics* **29,** 891–897.

Zema M., Domeneghetti M. C., Molin G. M., and Tazzoli V. (1997) Cooling rates of diogenites: A study of Fe^{2+}-Mg ordering in orthopyroxene by single-crystal x-ray diffraction. *Meteor. Planet. Sci.* **32,** 855–862.